2015

Computational Modeling of Cardiac Biomechanics

Amir Nikou
University of Kentucky, amirnikou@gmail.com

STUDENT AGREEMENT:

I represent that my thesis or dissertation and abstract are my original work. Proper attribution has been given to all outside sources. I understand that I am solely responsible for obtaining any needed copyright permissions. I have obtained needed written permission statement(s) from the owner(s) of each third-party copyrighted matter to be included in my work, allowing electronic distribution (if such use is not permitted by the fair use doctrine) which will be submitted to UKnowledge as Additional File.

I hereby grant to The University of Kentucky and its agents the irrevocable, non-exclusive, and royalty-free license to archive and make accessible my work in whole or in part in all forms of media, now or hereafter known. I agree that the document mentioned above may be made available immediately for worldwide access unless an embargo applies.

I retain all other ownership rights to the copyright of my work. I also retain the right to use in future works (such as articles or books) all or part of my work. I understand that I am free to register the copyright to my work.

REVIEW, APPROVAL AND ACCEPTANCE

The document mentioned above has been reviewed and accepted by the student's advisor, on behalf of the advisory committee, and by the Director of Graduate Studies (DGS), on behalf of the program; we verify that this is the final, approved version of the student's thesis including all changes required by the advisory committee. The undersigned agree to abide by the statements above.

Amir Nikou, Student

Dr. Jonathan F. Wenk, Major Professor

Dr. Haluk E. Karaca, Director of Graduate Studies

COMPUTATIONAL MODELING OF CARDIAC BIOMECHANICS

DISSERTATION

A dissertation submitted in partial fulfillment of the
requirements for the degree of Doctor of Philosophy in the
College of Engineering at the University of Kentucky

By
Amir Nikou
Lexington, Kentucky
Co-Directors: Dr. Jonathan F. Wenk, Professor of Mechanical Engineering
and Dr. Keith Rouch , Professor of Mechanical Engineering
Lexington, Kentucky

ABSTRACT OF DISSERTATION

COMPUTATIONAL MODELING OF CARDIAC BIOMECHANICS

The goal of this dissertation was to develop a realistic and patient-specific computational model of the heart that ultimately would help medical scientists to better diagnose and treat heart diseases. In order to achieve this goal, a three dimensional finite element model of the heart was created using magnetic resonance images of the beating pig heart. This model was loaded by the pressure of blood inside the left ventricle which was measured by synchronous catheterization. A recently developed structurally based constitutive model of the myocardium was incorporated in the finite element solver to model passive left ventricular myocardium. Additionally, an unloading algorithm originally designed for arteries was adapted to estimate the stress-free geometry of the heart from its partially-loaded geometry obtained from magnetic resonance imaging. Finally, a regionally varying growth module was added to the computational model to predict eccentric hypertrophy of the heart under various pathological conditions that result in volume overload of the heart. The computational model was validated using experimental data obtained from porcine heart such as in vivo strains measured from magnetic resonance imaging.

KEYWORDS: Computational Modeling, Finite Element Modeling, Cardiac Biomechanics, Magnetic Resonance Imaging, In Vivo Heart

Amir Nikou

Student's Signature

December 2015

Date

COMPUTATIONAL MODELING OF CARDIAC BIOMECHANICS

By

Amir Nikou

(Jonathan F. Wenk)
Co-Director of Dissertation

(Keith Rouch)
Co-Director of Dissertation

(Haluk E. Karaca)
Director of Graduate studies

(December 2015)

To my wife *Elaheh* and my daughter-to-be *Parmiss*

TABLE OF CONTENTS

LIST OF TABLES

LIST OF FIGURES

Chapter One: Introduction

According to CDC (Centers for Disease control and Prevention), heart diseases are the leading cause of death in the US (611,105 death in 2013). Common heart diseases are CAD (Coronary Artery Disease), CHF (Congestive Heart Failure), Cardiomyopathy (weak heart muscles), Arrhythmias (irregular heartbeat), congenital heart defects and heart valve problems. In order to better understand the mechanics of the heart and its disorders, computational methods are being used increasingly to investigate healthy and diseased cardiac tissue. Realistic computational simulations of the heart are able to provide information that cannot be measured clinically and may help them to better diagnose and treat cardiac diseases. For instance, stress distributions in the heart affect cardiac remodeling, but such distributions are not clinically available. Biomechanical models of the heart offer detailed three-dimensional deformation, stress and strain fields that can supplement conventional clinical data. The final goal of such efforts is to develop validated 3D patient-specific models that could be used easily in a clinical setting [2-8].

The long term goal of this study is to develop a realistic and patient-specific computational model of the heart that would hopefully help medical researchers to better diagnose and treat heart diseases. This goal could be achieved by either adding new capabilities to the existing model or by replacing current sub-models with more elaborate and recently developed ones. These models can be validated by applying these techniques to analyze healthy and diseased hearts using in vivo data from animals. Initial development of such models could involve data acquisition techniques that might not necessarily be patient-friendly or patient specific. For example, ventricular pressure is recorded by inserting a pressure catheter inside the animal's heart or tagged MRI used for capturing the deformation of the myocardium, but the final validated computational model must be able to use clinically available data such as clinically measured pressure, volume and CINE MRI data.

The Finite Element Method (FEM) has proven to be a universal tool for the analysis of complex structures in engineering and with increasing computing power, different nonlinear problems can be treated more easily [9]. Bioengineers increasingly make use of FEM to simulate the heart at systole (active contraction or ejecting phase of cardiac cycle) and diastole (passive dilation or filling phase of cardiac cycle). There are a variety of FEM commercial packages that could be used in computational modeling of bioengineering problems. In the Computational Biomechanics Lab (CBL) here at UK, we use LS-DYNA (Livermore Software Technology Corporation, Livermore, CA). LS-DYNA is an explicit solver that gives the user the ability to embed complicated user defined material models as FORTRAN subroutines. Additionally, it could be easily coupled with LS-OPT (Livermore Software Technology Corporation, Livermore, CA) which is a multi-purpose optimizer that is used to identify material parameters of different soft tissue constitutive laws.

The objective of this dissertation was to improve technical aspects of the current computational model and apply them to new series of data sets to characterize material properties of healthy and diseased hearts. More specifically, in chapter 2, in order to improve the constitutive modeling of cardiac tissue, the current transversely isotropic constitutive law was replaced by a newly developed and structurally based one. In chapter 3, a previously developed numerical method for unloading arteries was adapted to unload the geometry of heart from the early-diastolic state (non-zero pressure) to a zero pressure reference state. Finally in chapter 5, a continuum growth model was incorporated in the finite element solver which can predict concentric and eccentric hypertrophy after imposing pressure and volume overload to the finite element model.

Chapter Two: Constitutive Modeling

Understanding the complex structure of myocardium has been the subject of many studies. See works by Young et al. [10] and Sands et al. [11] for example. Accordingly, different models of cardiac structure have been proposed to better understand its performance. For an account of some approaches to describe the structure of the heart see the study of Gilbert et al. [12]. A common approach in the engineering community is to consider the myocardium as layered sheets of myofibers, which have orientation angles that vary transmurally and depend on species. Streeter et al. made some of the first quantitative measurements of fiber orientation in canine ventricles [13]. Subsequent investigations showed that myocardial microstructure is composed of discrete layers which run transmurally across the ventricular wall (Figure 1) [14] [15]. LeGrice et al. provided a more detailed and systematic account of the architecture of these sheets [16].

After obtaining descriptions of the geometry and structure of the myocardium, the next step in understanding myocardial mechanics is the constitutive equations that characterize the material properties of myocardium. There are several proposed models for describing the elasticity of myocardium, which are generally classified as: isotropic, transversely isotropic and orthotropic models. Isotropic models are not appropriate in view of the morphology and structure of passive myocardium [17]. Most of the previous analyses of cardiac function were based on the assumption that the material properties of the heart are highly dependent on muscle fiber orientation, but independent of the direction in the plane transverse to the muscle fiber axis [18]. This is to say that the material properties of myocardium are symmetric about the myofiber axis, which is referred to as transversely isotropic. The models of Humphrey and Yin [19], Humphrey et al. [20], Guccione et al. [21], Costa et al. [22] and Kerckhoffs at el. [23] assume myocardium as a transversely isotropic material. While transversely isotropic models are based on biaxial tension tests of myocardium, the results from shear experiments showed that the resistance of myocardial tissue to simple shear loading in different planes is noticeably different. This suggests that myocardial tissue

in diastole is an orthotropic material with distinct material properties in orthonormal planes of symmetry [24].

Although transversely isotropic models have been used extensively in computational simulations of myocardium, which have led to great insights to the mechanics of the heart, they do not capture the distinct response of myocardium in the three mutually orthogonal planes. Therefore more recently, orthotropic models of passive myocardium have been proposed, which take into account the distinct material response in the mutually orthogonal planes. The pole-zero model of Hunter et al. [25], and the Fung type models of Costa et al. [22] and Schmid et al. [26] are among some of the proposed orthotropic models. These models are partly structurally based, relating to the fiber, sheet, and normal directions, and are partly phenomenological [17].

The most recent orthotropic model for passive myocardium was proposed by Holzapfel and Ogden [17]. We will refer to this as the H-O model. Holzapfel and Ogden treated the left ventricular myocardium as a non-homogeneous, thick-walled, nonlinearly elastic, and incompressible material. This model takes into account the muscle fiber, myocyte sheet, and sheet normal directions. Additionally, this model describes the general characteristics of the available biaxial and shear experimental data, as examined in detail in their study. The H-O model is invariant based, which makes it geometry independent, and is suitable to use within the finite element method [27]. Furthermore, it is consistent with standard inequalities required for considerations of convexity, strong ellipticity, and material stability[17].

Goktepe et al. [28] implemented the H-O model in order to perform a finite element analysis of a generic biventricular heart model subjected to physiological ventricular pressure. Wang et al. [29] made use of the H-O model in a finite element simulation of a human left ventricle (LV), where the geometry was determined from magnetic resonance imaging (MRI) data. Additionally, they investigated the sensitivity of the H-O model to parameterizing errors and compared the results with other constitutive models and experimental results from canine hearts. The Wang et al. group then introduced a modified H-O model, which takes into account the effect of residual stresses in

the myocardium [30]. In both of these studies, the material parameters that were used in the ventricular finite element simulations were obtained by fitting the H-O model to previously published simple shear test data from porcine myocardium [24]. Holzapfel and Ogden [17] first reported a set of parameters by fitting their model to this experimental data and then Goketpe et al. and Wang et al. independently reported their own sets of parameters from the same experimental data [28] and [29].

Other studies have also used the same set of material parameters to implement the H-O model in their simulations. For example, Baillargeon et al. [31] used the parameters of Goktepe et al. [28] to implement the H-O model in order to represent a proof-of-concept simulator for a four-chamber human heart model created from computed topography and MRI. Some studies have used modified forms of the H-O model that have less material parameters. In a sense, these models have made limited use of the structurally based constitutive model by using less material parameters from the original form. For example, Krishnamurthy et al. [32] used a transversely isotropic variation of the H-O model, which has only four material parameters, to build LV models. That study incorporated myofiber and sheet architecture obtained from diffusion tensor MRI of an isolated and fixed human organ-donor heart, and then transformed it to a patient specific geometric model.

Most recently, Gao et al. [33] investigated the feasibility of identifying parameters of the H-O model from non-invasive clinical measurements for healthy myocardium. They introduced an optimization scheme to first identify known parameters of a LV model by generating a set of synthetic strain data and then extended their optimization method to in-vivo models with clinical data. In this study in-vivo strain data from cine MRI, along with a set of population based pressure data rather than measured pressure, were used to identify material parameters.

To our knowledge, parameter identification of the H-O material law using animal-specific strain data from SPAMM (SPAtial Modulation of Magnetization) MRI and synchronous pressure catheterization data has not yet been investigated. In this study we make use of finite element

models, which employ the H-O material law, and the optimization scheme proposed by Gao et al. [33] to estimate the eight material parameters of the H-O model using in-vivo MRI and pressure data from four healthy porcine LVs. Additionally, the resulting End-Diastolic Pressure-Volume Relationship (EDPVR) of each LV is examined to further explore the influence of the H-O model. Finally, the results obtained from the H-O models are compared with finite element models that employed the widely used constitutive model of Guccione et al.[21], which were also determined by optimization.

The data used in the current study is from same animal cohort that was used in the study of Mojsejenko et al. [34]. The animals used in this work received care in compliance with the protocols approved by the Institutional Animal Care and Use Committee at the University of Pennsylvania in accordance with the guidelines for humane care (National Institutes of Health Publication 85-23, revised 1996). For detail, please see Mojsejenko et al.[34]. Briefly, 3D SPAMM was performed in order to assess regional wall strain in four healthy adult male pigs weighing approximately 40 kg. The endocardium and epicardium of the LV were contoured from the 3D SPAMM images (Fig. 3). The reference contours were generated at early-diastolic filling and the endocardium was also contoured at end-diastole in order to calculate LV volume. The LV strain, volume, and contour data were all generated from the 3D SPAMM images and matched with the simultaneous pressure measurements (Fig. 4). This ensures that the data used in this study is consistent in terms of space and time.

The finite element model generation procedure is also explained in detail previously [34]. The primary difference is that the current study focuses only on healthy left ventricular myocardium and the use of the H-O model. In short, the reference state was taken to be early diastolic filling because it represents a relatively stress-free state as a result of minimal LV pressure. The LV pressure that was recorded simultaneously during MRI was used as a pressure loading boundary condition (Fig. 2). FE models were generated by fitting the endocardial and epicardial contours derived from MRI with 3D surfaces (Rapidform; INUS Technology, Inc., Sunnyvale, CA).

Hexahedral trilinear elements (TrueGrid; XYZ Scientific, Inc., Livermore, CA, USA) were used to generate the finite element mesh of the myocardium (Fig. 5). A custom MATLAB code was used to assign a linear distribution of myofiber orientation and myocyte sheet angles to each hexahedral element. For myofiber orientation angles, a distribution of -37^o (at epicardium) to +83^o (at endocardium) with respect to the circumferential direction was used based on the study of Lee et al.[35] and myocyte sheet angles varied from -45^o (at epicardium) to +45^o (at endocardium) with respect to radial direction following the study of LeGrice et al.[16]. A homogeneous distribution of the fiber and sheet angles was assumed over the entire LV. The constitutive model outlined in the next section was coded as a user defined material subroutine that was implemented in the nonlinear FE solver LS-DYNA (Livermore Software Technology Corporation, Livermore, CA). An explicit (central difference) time integration scheme with adaptive time stepping for stability was used to conduct the FE simulations

The strain energy function per unit reference volume proposed for the H-O model is given by [17]:

$$\psi = \frac{a}{2b}\{exp[b(I_1 - 3)] - 1\} + \sum_{i=f,s} \frac{a_i}{2b_i}\{exp[b_i(I_{4i} - 1)^2] - 1\} + \frac{a_{fs}}{2b_{fs}}\left\{exp\left(b_{fs}I_{8fs}^2\right) - 1\right\} \quad (1)$$

where $a, b, a_f, b_f, a_s, b_s, a_{fs}$ and b_{fs} are the eight positive material constants (a parameters have dimensions of stress and contribute to the magnitude of the stress-strain curve while b parameters are dimensionless and contribute to the nonlinearity of the stress-strain curve). The contribution of isotropic terms is included in I_1, transversely isotropic terms in I_{4f}, I_{4s} and orthotropic terms in I_{8fs}.

The four invariants used in the strain energy function are defined as follows:

$$I_1 = tr(\mathbf{C}), \quad I_{4f} = \mathbf{f_0}.(\mathbf{Cf_0}), \quad I_{4s} = \mathbf{s_0}.(\mathbf{Cs_0}), \quad I_{8fs} = \mathbf{f_0}.(\mathbf{Cs_0}) \quad (2)$$

where f_0 and s_0 are unit vectors that define the myofiber direction and myocyte sheet direction, respectively (Fig. 5), and C is the right Cauchy-Green deformation tensor defined as (F is the deformation gradient tensor):

$$\mathbf{C} = \mathbf{F}^{\mathbf{T}}\mathbf{F} \tag{3}$$

In order to avoid numerical complications in the finite element analysis of myocardium, which is assumed to be a nearly incompressible or slightly compressible material, the concept of multiplicative decomposition of the deformation gradient tensor F is used. Consequently, the strain energy function and second Piola-Kirchohff stress tensor were also decomposed into volumetric (volume-changing) and isochoric (volume preserving) parts [27]:

$$\mathbf{F} = \left(J^{1/3}\mathrm{I}\right)\bar{\mathbf{F}} = J^{1/3}\,\bar{\mathbf{F}} \tag{4}$$

$$\mathbf{C} = \left(J^{2/3}\mathrm{I}\right)\bar{\mathbf{C}} = J^{2/3}\,\bar{\mathbf{C}} \tag{5}$$

where $J = \det(\mathrm{F})$ and the tensors $\bar{\mathrm{F}}$ and $\bar{\mathrm{C}}$ are the modified deformation gradient and modified right Cauchy-Green tensors, respectively. In the same way, modified invariants (shown with over bar) can be defined using $\bar{\mathrm{C}}$ instead of C in their original definition.

The unique decoupled representation of the strain energy function is defined in the form[27]:

$$\psi(\mathbf{C}) = \psi_{vol}(J) + \psi_{iso}(\bar{\mathbf{C}}) \tag{6}$$

or when the strain energy is written as a function of the invariants:

$$\psi\left(I_1, I_{4f}, I_{4s}, I_{8fs}\right) = \psi_{vol}(J) + \psi_{iso}\left(\bar{I}_1, \bar{I}_{4f}, \bar{I}_{4s}, \bar{I}_{8fs}\right) \tag{7}$$

The first part of Eq. (7) is the purely volumetric contribution to ψ and in the case of incompressibility it denotes a Lagrange contribution and enforces the associated kinematical constraint[36]. In the current computational implementation, the volumetric contribution is defined by Eq. (8), where K is the bulk modulus and J is the Jacobian of the deformation gradient tensor[5]. A penalty method was used to enforce the near incompressibility condition.

$$\psi_{vol}(J) = \frac{K}{2}(J-1)^2 \tag{8}$$

The second part of Eq. (7) is the purely isochoric contribution to ψ and its representation is the same as Eq. (1), but with the invariants replaced with their corresponding modified invariants. The

second Piola-Kirchoff stress tensor is defined as the sum of the purely volumetric and purely isochoric parts:

$$\mathbf{S} = \mathbf{S}_{\text{vol}} + \mathbf{S}_{\text{iso}} \tag{9}$$

Using the well-known relation $\mathbf{S} = 2\frac{\partial \psi(\mathbf{C})}{\partial \mathbf{C}}$ we have:

$$\mathbf{S}_{vol} = 2\frac{\partial \psi_{vol}}{\partial \mathbf{C}} = K(J-1)J\mathbf{C^{-1}} \tag{10}$$

$$\begin{aligned}\boldsymbol{S}_{iso} = 2\frac{\partial \psi_{iso}}{\partial \mathbf{C}} = J^{-\frac{2}{3}}\Big\{ & a\,exp\big(b(\bar{I}_1 - 3)\big)\left(I - \frac{1}{3}\bar{I}_1\bar{\mathbf{C}}^{-1}\right) \\ & + 2a_f(\bar{I}_{4f} - 1)exp\left(b_f(\bar{I}_{4f} - 1)^2\right)\left(\mathbf{f_0}\otimes\mathbf{f_0} - \frac{1}{3}\bar{I}_{4f}\bar{\mathbf{C}}^{-1}\right) \\ & + 2a_s(\bar{I}_{4s} - 1)exp(b_s(\bar{I}_{4s} - 1)^2)\left(\mathbf{s_0}\otimes\mathbf{s_0} - \frac{1}{3}\bar{I}_{4s}\bar{\mathbf{C}}^{-1}\right) \\ & + a_{fs}\bar{I}_{8fs}\,exp\left(b_{fs}{\bar{I}_{8fs}}^2\right)\left(\mathbf{f_0}\otimes\mathbf{s_0} + \mathbf{s_0}\otimes\mathbf{f_0} - \frac{2}{3}\bar{I}_{8fs}\bar{\mathbf{C}}^{-1}\right)\Big\}\end{aligned} \tag{11}$$

A widely used transversely isotropic constitutive law developed by Guccione et al. was chosen to compare to the results of the H-O model [21]. In this model, the Fung-type exponential relation of strain energy for passive myocardium is as follows:

$$\psi = \frac{1}{2}\mathrm{C}\left(\mathrm{e}^{\mathrm{Q}} - 1\right) \tag{12}$$

with transverse isotropy given by:

$$\mathrm{Q} = \mathrm{b_f}{\mathrm{E_{11}}}^2 + \mathrm{b_t}\left({\mathrm{E_{22}}}^2 + {\mathrm{E_{33}}}^2 + {\mathrm{E_{23}}}^2 + {\mathrm{E_{32}}}^2\right) + \mathrm{b_{fs}}\left({\mathrm{E_{12}}}^2 + {\mathrm{E_{21}}}^2 + {\mathrm{E_{13}}}^2 + {\mathrm{E_{31}}}^2\right) \tag{13}$$

where the constants C, $\mathrm{b_f}$, $\mathrm{b_t}$ and $\mathrm{b_{fs}}$ are material parameters, $\mathrm{E_{11}}$ is the Green-Lagrange strain in the fiber direction, $\mathrm{E_{22}}$ is the sheet normal strain, $\mathrm{E_{33}}$ is the strain in the sheet direction and the rest are shear strains. For this model again we make use of decoupling the strain energy function into volumetric and isochoric parts. The final form of the Second Piola-Kirchoff stress is derived by taking the derivative of the strain energy function with respect to the deformation:

$$\mathbf{S} = K(J-1)J\mathbf{C}^{-1} + 2J^{-2/3}Dev\left(\frac{\partial \bar{\psi}}{\partial \bar{\mathbf{C}}}\right) \tag{14}$$

where near incompressibility is also enforced with a penalty method and Dev is deviatoric projection operator:

$$\mathrm{Dev}(*) = (*) - \frac{1}{3}([*]:\mathbf{C})\mathbf{C}^{-1} \tag{15}$$

The user defined material subroutine for this model was previously developed by Sun et al. [37]. The multi-step optimization scheme proposed by Gao et al. [33] was used to estimate the eight material parameters of the H-O model. Optimization was performed in three steps by minimizing the two following objective functions in a specific sequence:

$$f_{O1} = \sum_{n=1}^{N} \sum_{i,j=1,2,3} \left(E_{ij,n} - \bar{E}_{ij,n}\right)^2 + (V - \bar{V})^2 \tag{16}$$

$$f_{O2} = \sum_{n=1}^{N} \sum_{i,j=1,2,3} \left(E_{ij,n} - \bar{E}_{ij,n}\right)^2 + \left(\frac{V - \bar{V}}{\bar{V}}\right)^2 \tag{17}$$

where n is the strain point within the myocardium, N is the total number of strain points, $E_{ij,n}$ and V are the FE predicted end-diastolic strain and end-diastolic LV cavity volume, respectively, and the corresponding over bar variables represent in-vivo measured values. A total of $N = 252$ points in the mid-wall of the LV FE model, along with 252 of the nearest LV points measured from MRI data, were chosen for generation of each objective function. Details of the multi-step optimization scheme are presented in the study of Gao et al. [33]. Briefly, in the first step all parameters are updated by optimizing two scaling factors C_a and C_b defined as follows and using f_{O1} (Eq. (16)) as the objective function.

$$a^{group} = C_a \times a_0^{group}, \qquad b^{group} = C_b \times b_0^{group} \tag{18}$$

where $a^{group} = \{a,\ a_f,\ a_s,\ a_{fs}\}$, $b^{group} = \{b,\ b_f,\ b_s,\ b_{fs}\}$ and a_0^{group}, b_0^{group} are an

initial set of available H-O parameters. In the current study, we chose the parameters fit by Wang et al. to simple shear tests of Dokos et al. [24] on porcine heart samples as a_0^{group} and b_0^{group}

(Table 1). In the second step a_f and b_f are optimized using f_{O2} as the objective function while enforcing the following two constraints:

$$a_f \geq 2a_s\,, \qquad b_f \geq 2b_s \tag{19}$$

Finally, in the third step, a and a_{fs} are updated by optimizing the scaling factor C_3 defined as follows and using f_{O1} as the objective function [33].

$$a = C_3 a\,, \qquad a_{fs} = C_3 a_{fs} \tag{20}$$

A single step optimization scheme using the objective function f_{O2} (Eq. (17)) was used to determine the four material parameters of the transversely isotropic model from Guccione et al. To minimize the objective function in each step of the multi-step scheme and single step scheme, a Genetic Algorithm (GA) technique was chosen as the optimization method using LS-OPT software (Livermore Software Technology Corporation, Livermore, CA). Nair et al. [38] have shown that GAs are robust for the optimization of cardiac material parameters in 3D models. Details of the genetic algorithm used in this study, along with a flow chart of the optimization procedure, are presented in the study of Mojsejenko et al. [34]. Briefly, for the multi-step scheme the design variables are C_a and C_b in first step, a_f, a_s, b_f and b_s in second step, and C_3 in third step. In the single step scheme the design variables are the the four material parameters (C, b_f, b_t and b_{fs}). Within each iteration of the optimization, the software LS-DYNA runs the FE simulations corresponding to each set of design variables, after which LS-OPT begins the optimization using Eq. (16) and Eq. (17) as objective functions.

After running the optimization with data from the four porcine cases, the final optimized material parameters from both constitutive models were used to generate end-diastolic pressure-volume relationship (EDPVR) curves for each case. To do this, the FE model of the LV was loaded with different end-diastolic pressures above and below the measured end-diastolic pressure to obtain the corresponding end-diastolic volumes. The method proposed by Klotz et al. [39], to estimate the EDPVR curve from a measured end-diastolic pressure and volume point, was used to generate a

physiological benchmark for comparison with the FE predicted EDPVR curves. The Klotz relation for end-diastolic pressure in mmHg versus end-diastolic volume in mL is

$$EDP = \alpha \, . \, EDV^{\beta} \tag{21}$$

where α and β are defined as

$$\beta = Log\left({}^{P_m}/_{30}\right)/Log\left({}^{V_m}/_{30}\right)$$

$$\alpha = 30/{V_{30}}^{\beta}$$

V_m and P_m are measured volume and pressure, respectively, V_{30} is the end-diastolic volume at an end-diastolic pressure of 30 mmHg, which is defined as

$$V_{30} = V_0 + (V_m - V_0)/(P_m/A_n)^{(1/B_n)}$$

$A_n = 28.2$, $B_n = 2.79$ and V_0 is the unloaded LV cavity volume or end-diastolic volume at pressure of 0 mmHg. In this study, instead of using an empirical identity that Klotz et al. developed to estimate LV volume at zero pressure [39], we used measured volume at early diastole, which is the closest to a zero pressure state as can be measured in-vivo. Additionally, the same value was used as the reference volume to build the FE models, which allows a more direct comparison to the Klotz et al. results.

In order to initially validate the implementation of the H-O model into our FE framework, the results of the simple shear experiments of Dokos et al. [24] were replicated using the H-O model in a FE simulation of a single element. Independent studies by Holzapfel and Ogden [17], Goktepe et al.[28], and Wang et al. [29] used these results to estimate sets of the eight material parameters. Here we used the H-O parameters from Goktepe et al. to simulate the simple shear FE model. As shown in Figure 6, there is very good agreement over the entire strain range between our FE results and the experimental data. Additionally, the sensitivity of the H-O model to different orientations of myocyte sheets was tested by calculating different components of stress for one of the simple shear cases shown in Figure 7 (fs shear). To do this, a single element was rotated about the fiber direction from -45 to +45 degrees and a fixed amount of shear (maximum amount of shear shown

in the plot of Figure 6) was applied to the element in each orientation angle. The results indicate changes in different components of stress as the sample is rotated (Fig. 7). Obviously, transversely isotropic models of myocardium would not account for such changes.

Table 2 shows the final results of the multi-step optimization, yielding eight material parameters of the H-O model for each case under investigation. The corresponding material parameters using the constitutive model of Guccione et al. are listed in Table 3. In order to compare the optimization results of the two constitutive models, the optimized parameters in Tables 2 and 3 were used to run FE simulations corresponding to each of the four LV cases. Then, the mean squared error (MSE) between FE predicted strains and MRI measured strains, using Eq. (22), was computed for each case (Table 4). It can be seen that the MSE values for cases 1 through 3 are in close agreement, differing by 3% - 7% from each other, whereas case 4 showed more deviation with a difference of 14%. The reason for these differences is discussed in the next section.

$$MSE = \sum_{n=1}^{N} \sum_{i,j=1,2,3} \left(E_{ij,n} - \bar{E}_{ij,n}\right)^2 \tag{22}$$

In order to better understand the influence of the sheet angles on the fit of the H-O models, all of the LV simulations were rerun with sheet angles that aligned with the radial direction, rather than varying by ± 45 degrees. As expected, the MSE values for the cases with the Guccione material law were unchanged, due to the transversely isotropic nature of the law. However, the MSE values for the cases with the H-O material law increased by 6%, meaning that the difference between the FE predicted and MRI measured strain increased, leading to a worse fit of the experimental data. This indicates that the H-O model is sensitive to the orthonormal basis that is used to describe the fiber, normal, and sheet directions and that more realistic sheet angles lead to a better fit between the model and experimental data.

As an additional step to qualitatively compare the results of the two constitutive models, the EDPVR curve was used, which is a powerful tool in both the medical and biomechanics

communities since it characterizes the passive properties of the ventricles. Furthermore, the parameter estimation in this study is based on measured strains, cavity volume and pressure at the end of diastole, which justifies the use of the EDPVR curve to have a qualitative understanding of the two different constitutive models. As a benchmark for the EDPVR curve, we used the method developed by Klotz et al. [39]. They proposed a single-beat approach to estimate the whole EDPVR from one measured volume-pressure point. Figures 8 through 11 show the EDPVR curves obtained using the H-O model, model of Guccione et al., and the physiological benchmark curve using the Klotz et al. method. These figures clearly show that the H-O model gives better agreement with the Klotz curve.

The goal of this study was to quantify the eight material parameters of the structurally based H-O constitutive model using in-vivo strain and synchronous pressure data from four healthy porcine LV cases. The parameter estimation was achieved by using a combination of FE simulations and a recently developed optimization scheme specifically for the H-O model [33]. Additionally, four material parameters for the widely used phenomenological constitutive model developed by Guccione et al. [21] were obtained and the corresponding results compared.

Based on the results of our study, the H-O model was shown to produce a more realistic estimate of the ventricular mechanics, by generating a more physiological EDPVR curve. Figures 8 through 11 show the EDPVR curves obtained using both constitutive models, as well as a physiological benchmark curve using the method by Klotz et al. [39]. A common trend in all four cases is that the EDPVR curve predicted by the H-O model is closer to the Klotz curve, indicating a physiological EDPVR. The slope of the EDPVR curve is an indicator of the overall stiffness of the myocardium during the passive phase of the cardiac cycle. A closer look at Figures 8 through 11 reveals that the H-O model also predicts the myocardial stiffness more exactly than model of Guccione et al. over the entire range of volumes. This is very advantageous, since this was achieved by fitting the constitutive model to measured data only from end-diastole.

Considering that the identical fiber orientation angles were used in both models, one reason the results of the H-O model is more realistic is that the mathematical formulation takes into account the myocyte sheet angles, which leads to more realistic description of the morphology of the myocardium. The final results in the form of MSE values for the two constitutive laws (Table 4) indicate that MSEs are very close, but the H-O model has MSE values that are slightly higher than the Guccione model. One explanation is that in this study we are assigning *assumed* distributions of myofiber orientation and myocyte sheet angles to a structurally based model. Structurally based models sense the material only from its assigned architecture, unlike phenomenological models that follow the general behavior of material. This was also observed when the simulations that used the H-O model were assigned more realistic sheet architecture. Specifically, when assigning the assumed variation in sheet angles versus the case when the sheet angles were assumed to be directed radially toward the center of LV, the MSE values decreased indicating a better fit. Obviously, improvement in the sheet angle distribution does not affect the results of transversely isotropic models. Based on the results of four LV cases in this study, the best way to incorporate myocardium architecture when using the H-O model (or any other structurally based constitutive law) is by mapping animal-specific, real fiber and sheet angles (e.g. from DTMRI) to the FE model. This is the subject of future investigations for the authors.

In some studies, the material parameters were obtained by fitting the H-O model to simple shear or biaxial experimental data of ex-vivo heart tissues and then used to simulate beating LVs, (for example see [28] [29] [32]). However, in the current study the parameters of the H-O model were quantified using in-vivo strain data from MRI. Despite some studies that used reduced forms of the H-O model with less material parameters (for example see [32]), in the current study the proposed optimization scheme of Gao et al. was used to quantify all eight material parameters. In addition, by using a larger number of 3-D strain data points (252 points, all 6 components of the strain tensor at each point) in the optimization procedure, this adds to the reliability of the optimization results in this study. In the work by Gao et al., a smaller number of strain points were used in the

optimization, and radial strains were not used to quantify the material parameters of the H-O model. In addition to the quantity of experimental data, the 3D SPAMM MRI data used in this study are more accurate at capturing myocardial deformation than the cine MRI data used in previous studies. Furthermore, in this study synchronous pressure catheterization data was used to load the FE model, while in other implementations of the H-O model average or population based pressure data was used [29] [33].

There are some limitations associated with this implementation of the constitutive models. One limitation is that the FE models lack the pericardium and RV. The absence of the RV decreases the accuracy of estimated parameters as discussed previously by Mojsejenko et al. [34]. Another limitation is using early diastolic filling, where LV is under minor loading, as the reference state of the FE models. Additionally, the residual active tension in the myocardium is not taken into account, which could be a source of error in the parameter estimation. The techniques proposed by Krishnamurthy et al. [32] and Xi et al.[40] will be used in future investigations to incorporate these effect to the FE model used to estimate parameters. Despite these limitations, the implementation of the H-O model in the current study demonstrates enhanced capabilities for fitting constitutive models using in-vivo data.

Table 1: Parameters of Wang et al. [29] used as the initial set of parameters in step 1

$a\ (kPa)$	b	$a_f(kPa)$	b_f	$a_s(kPa)$	b_s	$a_{fs}(kPa)$	b_{fs}
0.2362	10.810	20.037	14.154	3.7245	5.1645	0.4108	11.300

Table 2: Optimized parameters of H-O model to in-vivo healthy myocardium of four cases under investigation

Parameters	$a\ (kPa)$	b	$a_f(kPa)$	b_f	$a_s(kPa)$	b_s	$a_{fs}(kPa)$	b_{fs}
Case 1	1.055	20.85	4.659	0.23	0.224	0.11	1.833	21.80
Case 2	2.401	54.05	0.271	151	0.128	47.33	4.176	56.50
Case 3	0.6542	20.85	6.959	2.15	3.407	1.05	1.219	21.79
Case 4	1.780	37.83	0.1435	200.2	0.012	8.72	3.096	39.55

Table 3 : Optimized parameters of Guccione et al. model to in-vivo healthy myocardium of four cases under investigation

Parameters	$C\ (kPa)$	B_f	B_t	B_{fs}
Case 1	0.493	38.06	4.11	45.07
Case 2	0.589	98.44	12.36	26.45
Case3	0.225	93.78	11.86	18.36
Case 4	0.391	92.6	1.11	49.27

Table 4: MSE between in-vivo MRI and FE predicted strains using two constitutive models and optimized parameters from Tables 2 and 3

	MSE, Holzapfel-Ogden model	MSE, Guccione et al. model
Case 1	7.55	7.11
Case 2	15.37	14.87
Case 3	10.90	10.17
Case 4	10.13	8.64

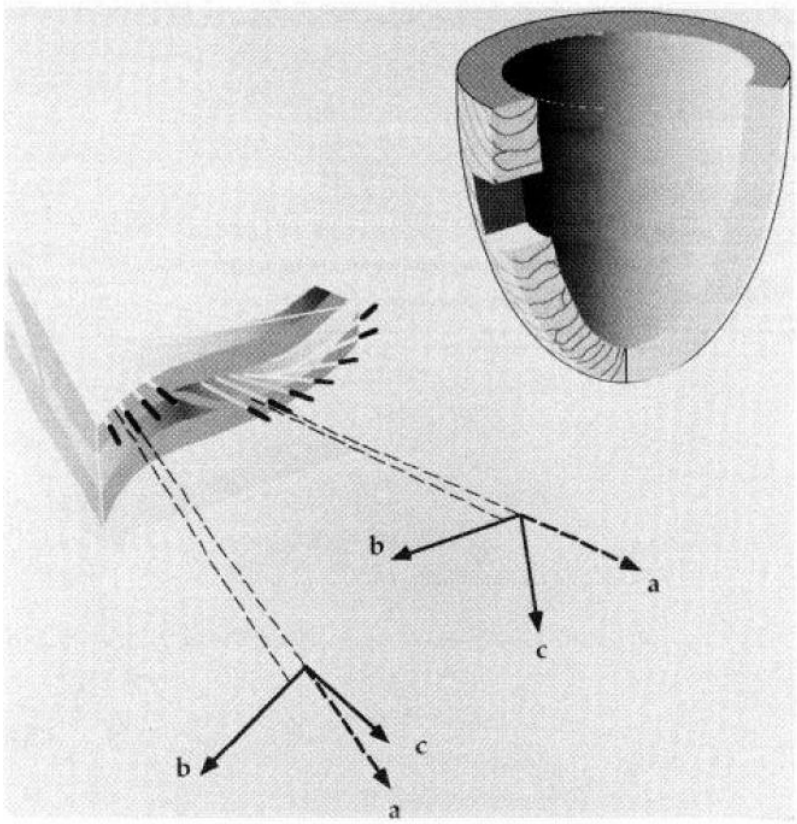

Figure 1: Micro structure of myocardium. Vectors **a**, **b** and **c** define local material axes, respectively: fiber, sheet and normal directions [1]

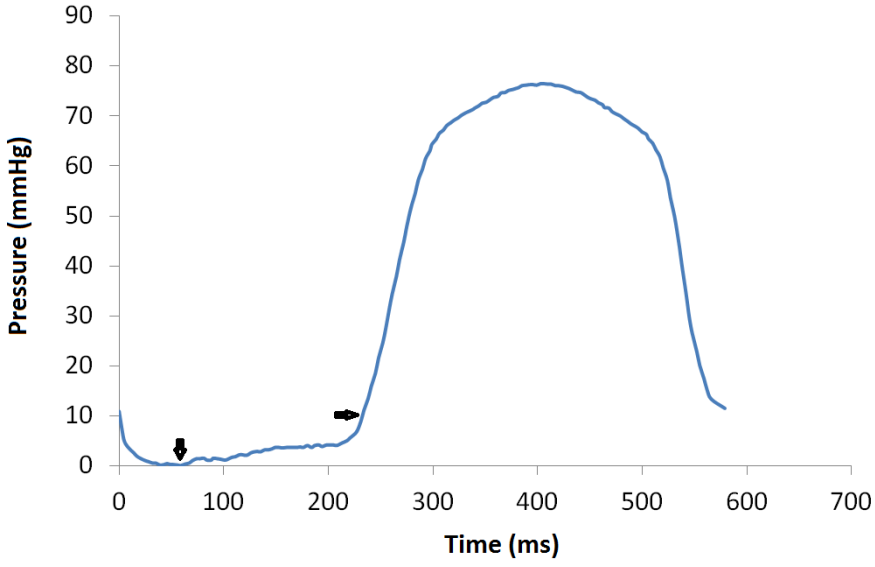

Figure 2 : Pressure versus time collected from LV catherization of case 1. Indicated points are early-diastolic and end-diastolic time points.

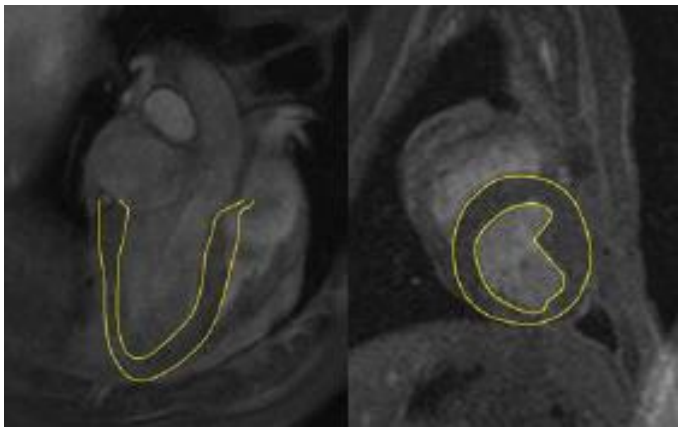

Figure 3: MRI data were contoured and converted to surface geometry and finite element meshes were projected to the surfaces

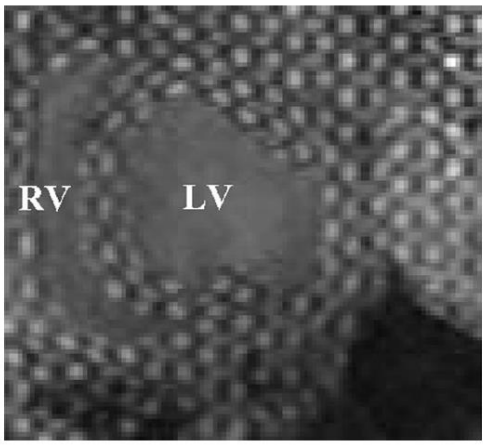

Figure 4: Short axis view of 3D SPAMM images from case 1 at end diastole

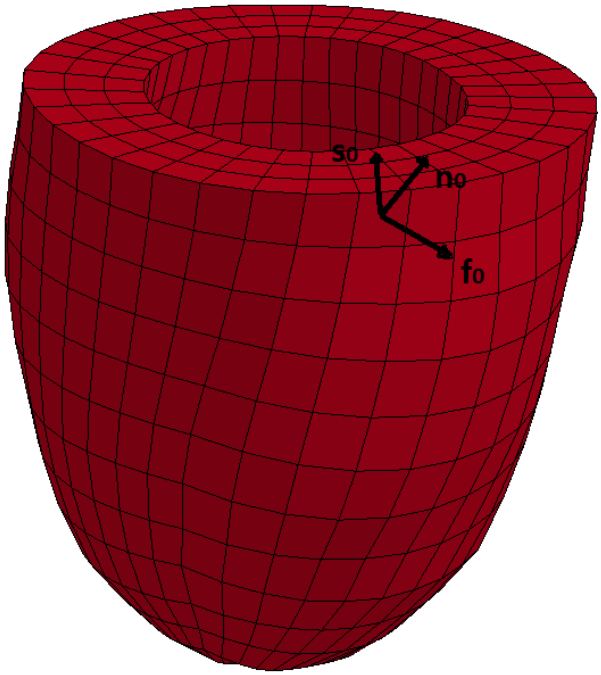

Figure 5: Finite Element model of porcine LV for case 1, the frame shows local fiber ($\mathbf{f_0}$), sheet ($\mathbf{s_0}$) and normal ($\mathbf{n_0}$) directions in H-O model schematically.

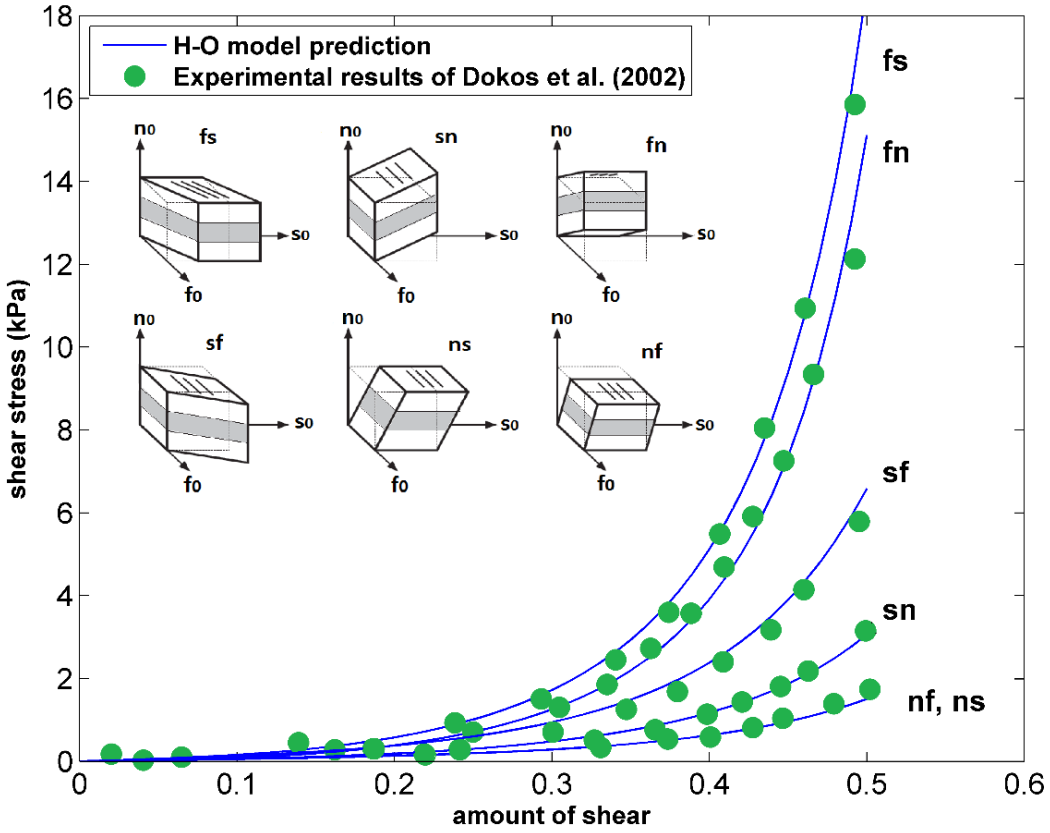

Figure 6: Fit of the H-O model (solid lines) to the experimental data (circles) of Dokos et al.[24]. Material parameters of Goktepe et al. [28] used for H-O model.

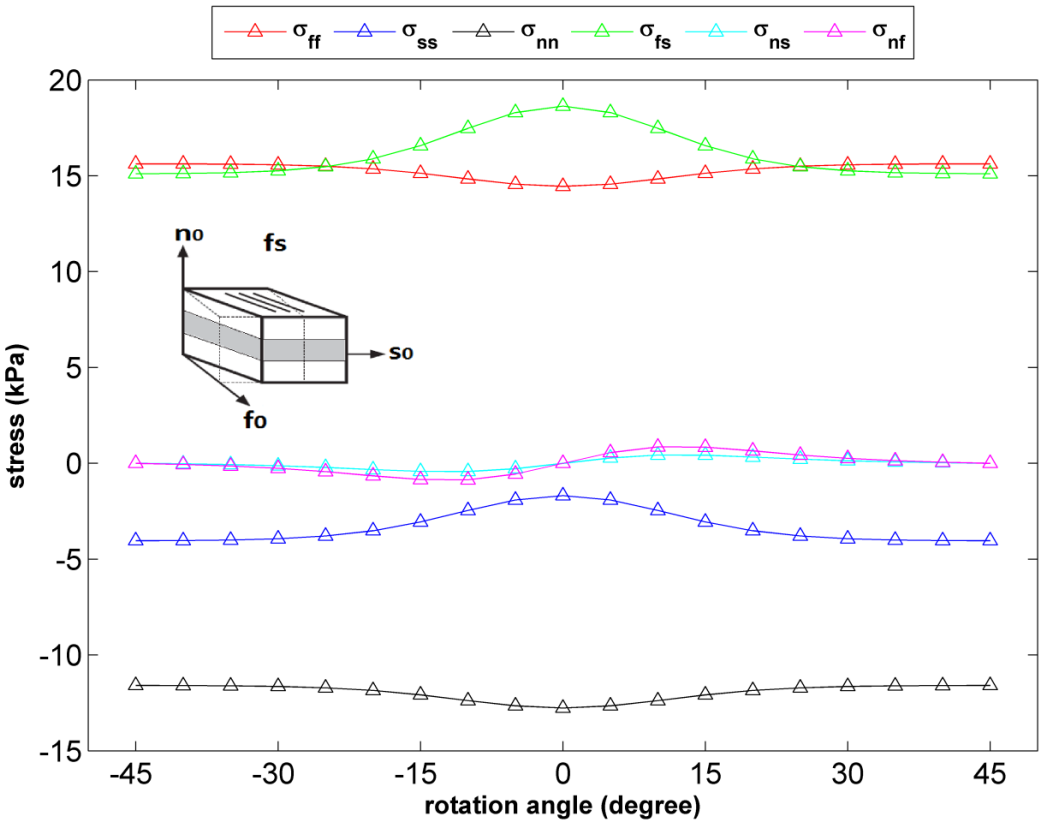

Figure 7: Variation of stress components vs. orientation angle of single element (rotation about fiber direction) for one simple shear case (fs shear), the amount of shear applied on the element is fixed (=0.5).

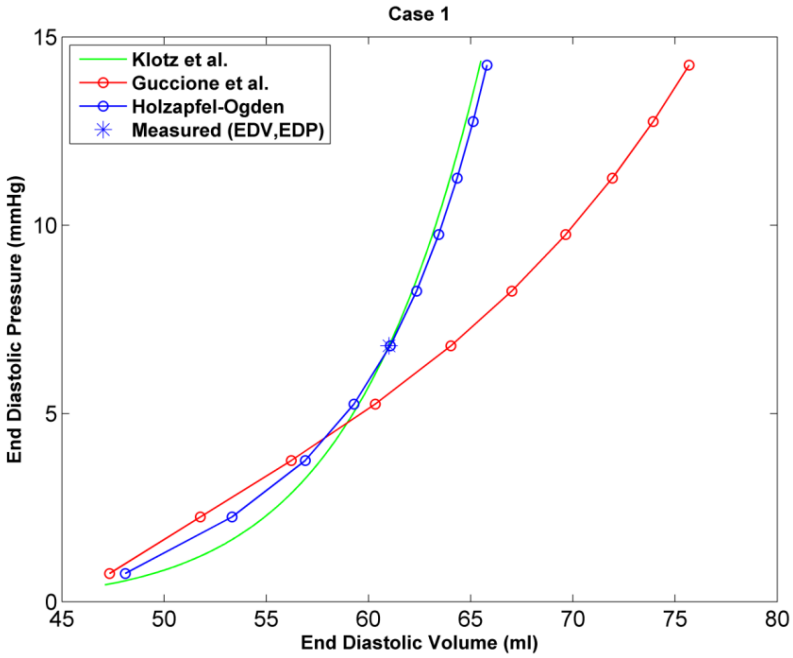

Figure 8: EDPVR curve predicted by H-O model (blue), model of Guccione et al. (red) and method of Klotz et al. (green) as a physiological benchmark for case 1.

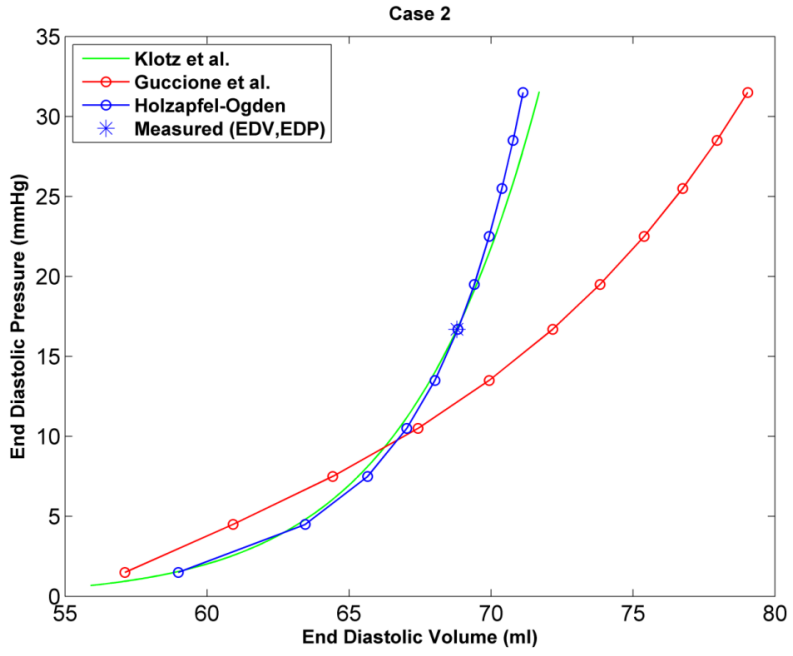

Figure 9: EDPVR curve predicted by H-O model (blue), model of Guccione et al. (red) and method of Klotz et al. (green) as a physiological benchmark for case 2.

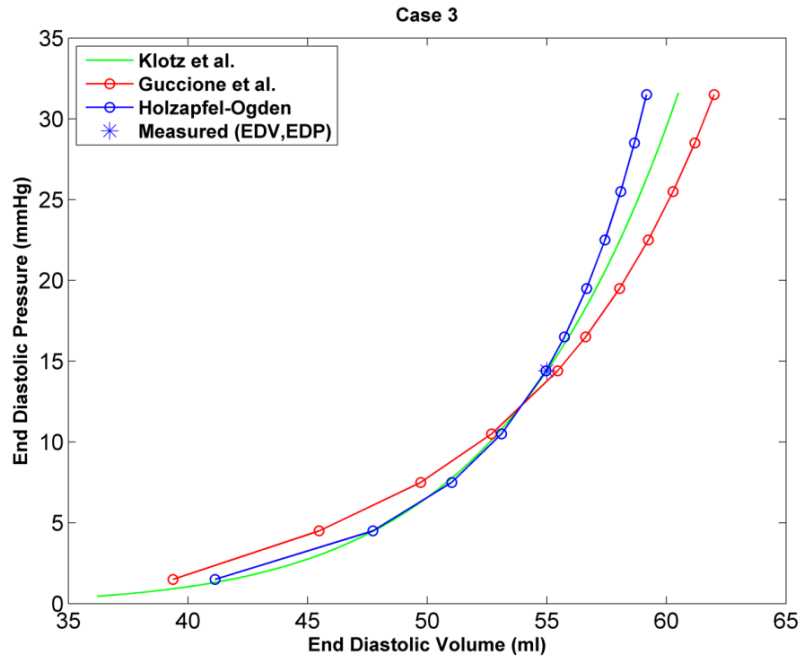

Figure 10: EDPVR curve predicted by H-O model (blue), model of Guccione et al. (red) and method of Klotz et al. (green) as a physiological benchmark for case 3.

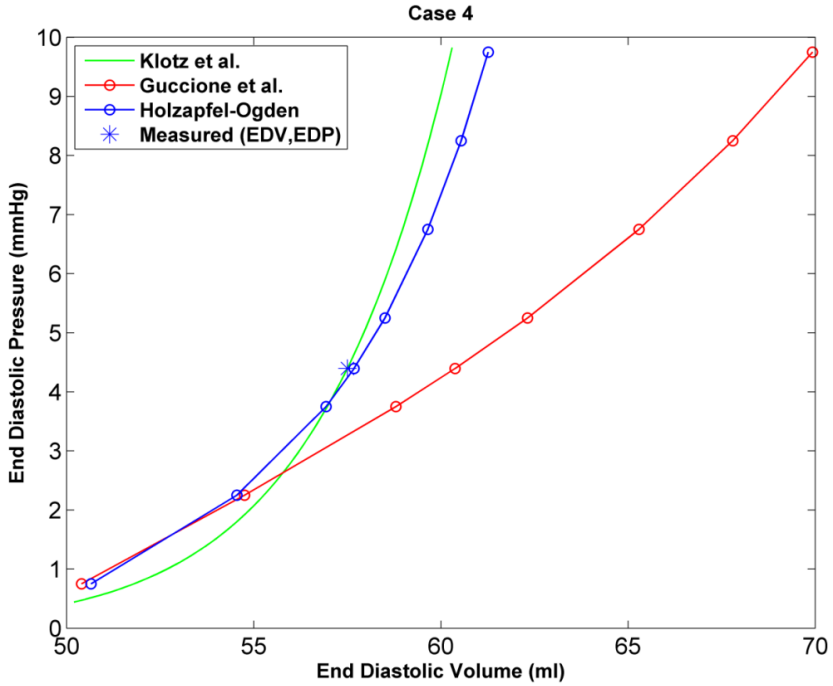

Figure 11: EDPVR curve predicted by H-O model (blue), model of Guccione et al. (red) and method of Klotz et al. (green) as a physiological benchmark for case 4.

Chapter Three: Estimating Reference Configuration of the Heart

In order to create realistic computational models, researchers increasingly make use of magnetic resonance images (MRI) of the heart. In addition to capturing geometric features, special imaging sequences (such as tagged MRI) can be used to obtain a realistic description of myocardial deformation. This deformation field can eventually be used, in combination with finite element (FE) modeling and numerical optimization, to quantify the nonlinear material properties of the heart.

In FE methods (and other computational modeling methods as well), using a good estimate of the initial unloaded configuration is a key factor to obtain realistic deformation and distribution of stress. Such a reference state rarely exists during a normal cardiac cycle, due to a continuously present physiological pressure load. Consequently, MR images of the heart, which are used to construct FE models, can only represent loaded states. Different assumptions in the literature have been made to improve the approximation of using a loaded configuration as a reference state. Some studies have used the early-diastolic geometry of the heart (or ventricles) as the reference state of their FE model [7], [41], while others have used the mid-diastolic state [42]. In the majority of these cases the specific reference state was chosen because the LV pressure was "at a minimum". However, the ventricle was still partially loaded, i.e., none of these states represent the true zero pressure or stress free configuration of the heart [39].

Several methods have been suggested to estimate the unloaded configuration of a deformed structure. In one such approach, the unloaded configuration of a soft structure is identified from a known deformed configuration by using conventional finite elasticity balance equations along with a solution procedure that treats the reference configuration as the unknowns [43]. Another method is based on a multiplicative decomposition of the deformation gradient tensor, which is typically useful in growth and remodeling studies [44]. There are also less direct methods, which are based on iterative schemes that are coupled to parameter identification methods for evaluating

biomaterials [32]. Recently, Bols et al. proposed the backward displacement method which is able to solve the inverse problem of finding the unloaded configuration based on fixed-point iterations [45]. The goal of that study was to assess the unloaded configuration of patient-specific blood vessels. The implementation of the method is straightforward and it is not computationally intensive compared to previously developed methods. Several of these unloading methods have been implemented in studies that focused on computational modeling of the cardiovascular system [30, 32, 46]. However, no studies have been conducted that investigate the effect of utilizing an unloaded versus partially loaded reference configuration when using FE modeling and optimization to predict the mechanical properties of the myocardium.

In our preliminary study, the method of Bols et al. [45] was adapted to unload the geometry of five healthy porcine left ventricle (LV) models, which were created from in-vivo MRI data that was contoured at early-diastole. This provided two FE models for each of the five cases, (1) with a reference geometry based on early-diastole and (2) with a reference geometry that is based on the estimated unloaded state. In order to study the effect of unloading, passive material parameters of the myocardium were identified using a technique that uses a combination of MRI/pressure data, FE modeling, and numerical optimization [34]. The ultimate goal was to see if the choice of an early-diastolic (partially loaded) or unloaded reference state affects the predicted material properties. After each case was processed with the optimization technique, the resulting properties were then used in the simulation of equi-biaxial extension, in order to visualize the predicted fiber and cross-fiber stiffness.

In this study, five healthy adult male pigs weighing approximately 40 kg were used in order to assess in-vivo cardiac function (Table 5). The animals used in this work received care in compliance with the protocols approved by the Institutional Animal Care and Use Committee at the University of Pennsylvania in accordance with the guidelines for humane care (National Institutes of Health Publication 85-23, revised 1996). The data used in the current study is from the same animal cohort that was used in the study of Mojsejenko et al. [34]. Briefly, 3D SPAMM (SPAtial Modulation of

Magnetization) MRI was performed in order to assess regional wall strain and contours of the LV epicardium and endocardium. The reference contours were generated at early-diastolic filling and the endocardium was also contoured at end-diastole, in order to calculate LV volume. FE models were generated by fitting the endocardial and epicardial contours with 3D surfaces (Rapidform; INUS Technology, Inc., Sunnyvale, CA). Hexahedral trilinear elements (TrueGrid; XYZ Scientific, Inc., Livermore, CA, USA) were used to generate the finite element mesh of the myocardium. A custom MATLAB code was used to assign a linear distribution of myofiber orientation and myocyte sheet angles to each hexahedral element. For myofiber orientation angles, a homogeneous distribution of -37^{o} (at epicardium) to $+83^{o}$ (at endocardium) with respect to the circumferential direction was used based on the study of Lee et al. [35]. The strain, volume, and contour data were all generated from the 3D SPAMM images and matched with the simultaneous LV pressure measurements. This ensures that the data used in this study is consistent in terms of space and time. The LV pressure was used as a pressure loading boundary condition in the model (end-diastolic pressure for FE simulations in the material parameter estimation and early-diastolic pressure for FE simulations in the unloading routine). The constitutive model outlined in section 2.2 was coded as a user defined material subroutine that was implemented in the nonlinear FE solver LS-DYNA (Livermore Software Technology Corporation, Livermore, CA). An explicit (central difference) time integration scheme with adaptive time stepping for stability was used to conduct the FE simulations.

The passive material properties of the myocardium were assumed to be nearly incompressible and transversely isotropic with respect to the local myofiber direction. The diastolic mechanics are described by the strain energy function for passive myocardium, in which a Fung-type exponential relation is used [21].

$$\psi = \frac{1}{2}\mathrm{C}\left(\mathrm{e}^{\mathrm{Q}} - 1\right) \tag{23}$$

With transverse isotropy given by

$$Q = b_f {E_{11}}^2 + b_t\left({E_{22}}^2 + {E_{33}}^2 + {E_{23}}^2 + {E_{32}}^2\right) + b_{fs}\left({E_{12}}^2 + {E_{21}}^2 + {E_{13}}^2 + {E_{31}}^2\right) \quad (24)$$

where the constants C, b_f, b_t and b_{fs} are material parameters, E_{11} is the Green-Lagrange strain in the fiber direction, E_{22} is the sheet normal strain, E_{33} is the strain in the sheet direction and the rest are shear strains. To enforce incompressibility, the strain energy function is decoupled into volumetric and isochoric parts. The final form of the Second Piola-Kirchoff stress is derived by taking the derivative of the strain energy function with respect to the deformation:

$$\mathbf{S} = K(J-1)J\mathbf{C}^{-1} + 2J^{-2/3}Dev\left(\frac{\partial \bar{\psi}}{\partial \bar{\mathbf{C}}}\right) \quad (25)$$

where near incompressibility is enforced with a penalty method and Dev is deviatoric projection operator:

$$\mathrm{Dev}(*) = (*) - \frac{1}{3}([*]:\mathbf{C})\mathbf{C}^{-1} \quad (26)$$

A Genetic algorithm (GA) technique was chosen for the optimization, and was performed using the software LS-OPT (Livermore Software Technology Corporation, Livermore, CA). In a previous study GAs were found to be a robust method for optimizing cardiac material parameters in 3D models. Details of the method, which was also used in the current study, can be found in [34]. Briefly, the material parameters in Equations 23 and 24 (C, b_f, b_t, b_{fs}) were optimized within the ranges previously reported for normal myocardium [47]. The objective function that was minimized during the optimization was taken to be the mean squared error (MSE) between MRI measured and FE predicted strains as well as the normalized difference in LV cavity volume, both at end-diastole. A total of N=252 points (centroids of midwall elements) were compared to the nearest LV points from the MRI data where strain was measured. The MSE was defined as

$$MSE = \sum_{n=1}^{N} \sum_{i,j=1,2,3} \left(E_{ij,n} - \bar{E}_{ij,n}\right)^2 + \left(\frac{V - \bar{V}}{\bar{V}}\right)^2 \quad (27)$$

where n is the strain point within the myocardium, N is the total number of strain points, $E_{ij,n}$ and V are the FE predicted end-diastolic strain and end-diastolic LV cavity volume, respectively, and the corresponding over bar variables represent in-vivo measured values.

In this study, the unloading of MRI derived geometry is dependent on the material parameters of the constitutive model incorporated in the FE solver, since multiple FE solutions are required to obtain the unloaded configuration [45]. Therefore, material parameter estimation and unloading of the geometry are coupled together. The outline of the two major steps that were used is as follows: in the first step, parameters of the passive constitutive law are estimated by using early-diastolic geometry (loaded configuration) as the reference configuration of the FE model. The details of the FE model and parameter estimation procedure are given in chapter 2. Clearly, the material parameters estimated at this step are dependent on the assumed reference configuration in the FE model, which is in a loaded state. In the second step, the unloaded configuration is obtained using material parameters estimated in the first step. In order to unload the LV geometry, the backward displacement method is used; in this method a given target geometry (early-diastolic geometry derived from MRI) and a load (early-diastolic pressure measured via catheterization) are used in a fixed point algorithm in which an iteratively updated displacement field is subtracted from the target geometry (Figure 12). The first estimate of the unloaded geometry was chosen to be the early-diastolic geometry and the final estimate was assumed to be the one that when loaded to the early-diastolic pressure, matches the target geometry best. In order to further refine the estimate of the unloaded geometry and material properties, these two steps were repeated until the unloaded geometry did not change. Specifically, the estimate of the unloaded geometry from the previous set of steps was used as the reference configuration of the FE model in the material parameter estimation process. Then, these updated properties were used to generate a new estimate of the unloaded geometry. A flowchart of the unloading-parameter estimation scheme is shown in Figure 13. On average, each case underwent three sets of material parameter estimation and unloading.

Parameter estimations for all cases converged to the optimized values in less than 30 iterations of the Genetic Algorithm and each set of the unloading scheme converged to the final estimate of unloaded configuration in less than 10 iterations (Figure 14). Each of the 5 cases had different levels of pressure at early-diastole (Table 5), which affected the amount of unloading that was estimated. For the cases when the early-diastolic pressure was low, the amount of unloading was less, as compared to when the pressure was high (Table 6). This is intuitive, since a low pressure causes the LV to be close to an unloaded state. The amount of unloading ranged from 3.2 mL to 11.15 mL, which is directly related to the level of early-diastolic pressure and material stiffness.

The optimized material parameters before and after unloading are listed in Table 6. It should be noted that the agreement between the FE model predict strain and MRI measured strain (as indicated by the MSE) was comparable in each of the 5 cases, when comparing the results of using the loaded vs. unloaded reference state. It is clear that in most cases, the material parameters changed noticeably after unloading. Since the contribution of the first parameter (C) and other parameters (b_f, b_t and b_s) in the strain energy function (Equation 23) are coupled it is difficult to infer a meaningful conclusion, regarding changes in stiffness, only from their numeric values. In order to better visualize the effects of unloading the LV on predictions of myocardial stiffness, we used the estimated parameters to plot stress vs. strain curves of the material based on simulated equi-biaxial extension tests. From these plots, it is clear that in all cases, the computational model predicts a softer passive myocardium after unloading. Case 1 showed the smallest change in stiffness, but this was also the case that unloaded the least. The other cases showed a larger change in stiffness, but converged to the final values after 3 sets of the unloading scheme.

The average stress in the LV wall also changed due to unloading (Table 7 and Figure 15). The global average of stress in the myofiber direction decreased in all of the cases, except for case 1. Since the material properties of the myocardium became less stiff, due to using the unloaded

reference geometry in the optimization scheme, the stress decreased even though the ventricles are loaded to the same end diastolic pressure.

The stress-strain curves in Figures 16 through 20 are used merely as an estimate of overall myocardial stiffness since in reality, the deformation and loading of myocardium is more complicated than a biaxial stress-strain state. The general trend in all cases is that using an unloaded configuration for the LV FE model results in a softer passive myocardium. The decrease in stiffness, when using the unloaded configuration, could be explained as follows: in the parameter estimation process, the FE solver inflates the reference configuration of the LV to the end-diastolic pressure and then optimum parameters are chosen in a way such that the deformation in the FE model at the end-diastolic point matches the best with in-vivo measured strains. For unloaded models, a relatively larger deformation is required to reach to the measured deformation field because the loaded (not-unloaded) models have already undergone some deformation without any applied pressure load. This means that the unloaded models undergo larger deformation under the same load, which is only possible if the material is softer.

The material parameters determined in the current study showed variability from case to case (Table 6). It should be noted that this type of variability has been observed in several previous studies of normal myocardium, where the values of C, b_f, b_t, and b_s varied by as much as a factor of 5 within the same group of animals [47-49]. Given the results of the current study, as well as previous studies, there appears to be natural variability in ventricular stiffness within an animal group.

Figure 21 shows myofiber stress vs. strain curves from the simulated equi-biaxial extension test using the results of this study (before and after unloading) and a previous study that used four isolated arrested pig hearts undergoing passive inflation of the left ventricle [47]. In that study, a similar approach was used to estimate the passive material parameters, i.e., using a combination of tagged MRI/pressure measurements, FE modeling, and numerical optimization. Clearly, after unloading the LV model, the myofiber stiffness is closer to the stiffness predicted by the previous

study, which used unloaded (isolated hearts) as the reference configuration of the LV models. This indicates that unloading the heart does have a significant influence on the determination of the myocardial stiffness, when using the combined MRI/modeling approach.

To investigate the effect of unloading on predicting the pressure-volume (PV) relationship of the LV, the experimentally measured PV data for one case (case 4) was compared with the corresponding FE predicted values (Figure 22). It is clear that the unloaded model resulted in a more accurate prediction of the PV data compared to the early-diastolic reference state model.

There are several limitations associated with the presented work. The contribution of residual stresses in the myocardial tissue is not taken to account, even though the effect of these stresses are relatively small in diastole [30]. Moreover, the transversely isotropic constitutive law used in this study is not completely consistent with the morphology and structure of myocardium [24]. In future works, this material law will be replaced with a structurally based material law [17]. Additionally, in the current study, average myofiber angles in porcine heart were assigned to the myocardium. In the future, animal specific distribution of myofiber angles obtained from diffusion tensor images (DTI) will be used [50].

In this study, in-vivo MRI and pressure catheterization data of five healthy porcine heart were used to measure the deformation and create 3D FE models. The LV models were numerically unloaded and the passive parameters of the material law embedded in FE solver were estimated using both the loaded and unloaded reference state models. Final results indicate that the unloaded configuration results in better approximation of myocardium response that is in good agreement with previous studies. Specifically, passive stiffness of myocardium decreases by unloading the reference state of the model, which is initially taken from MRI as the early-diastolic state. This study shows that numerically unloading the MRI-derived model is an essential step toward developing a more realistic representation of LV mechanical function. This will play a key role

when applying these approaches to build patient-specific computational models for assessing myocardial health.

Table 5: Five studied cases and their physiological characteristics

Case #	Early-diastolic pressure (kPa)	End-diastolic pressure (kPa)	Early-diastolic volume (mL)	End-diastolic volume (mL)
1	0.04	0.90	47.1	61.0
2	0.60	2.78	57.6	71.6
3	0.56	2.22	54.7	68.8
4	0.54	1.92	35.9	57.0
5	0.94	2.17	49.9	56.1

Table 6: Results of the material parameter estimation. For each case, the first and second row show optimization results when loaded and unloaded geometries were used as the reference configuration of the FE model, respectively.

Case #	FE reference volume (mL)	$C\ (kPa)$	b_f	b_t	b_{fs}	MSE
1	47.1	0.493	38.06	4.11	45.07	7.11
	43.9	0.433	37.88	4.195	45.41	7.09
2	57.6	7.086	11.53	3.70	3.70	15.37
	50.3	0.208	79.21	24.94	9.83	15.26
3	54.7	0.589	98.44	12.36	26.45	14.87
	49.3	6.719	7.95	1.21	2.38	15.01
4	35.9	0.238	87.54	12.47	16.69	10.30
	24.75	0.343	29.41	4.62	5.46	10.53
5	49.9	3.914	49.42	1.00	12.05	5.39
	44.4	4.944	20.40	1.07	8.57	6.09

Table 7: Global avera ge of LV stress in the myofiber direction at end-diastole (kPa). Note, each case was loaded to the measured end diastolic pressure to generate the stress in the LV.

Case #	Before unloading	After unloading	% Decrease
1	1.42	1.42	0%
2	3.35	3.24	3.3%
3	3.33	3.14	5.7%
4	2.94	2.73	7.1%
5	4.08	3.56	12.7%

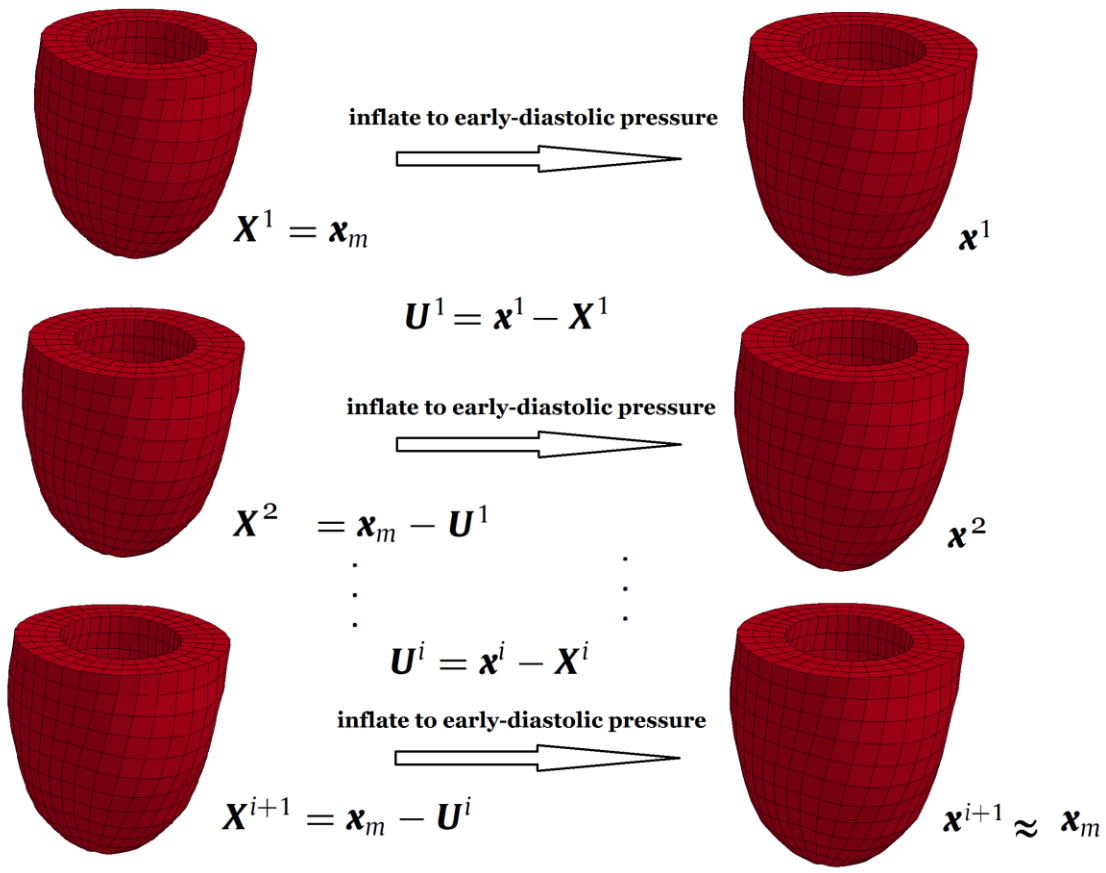

Figure 12: Backward displacement method applied to LV model. X represents nodal coordinates of consecutive estimates of unloaded geometry and x represents nodal coordinates of these estimates when inflated to early-diastolic pressure. x_m is the nodal coordinates of target geometry (MRI derived geometry at early-diastole)

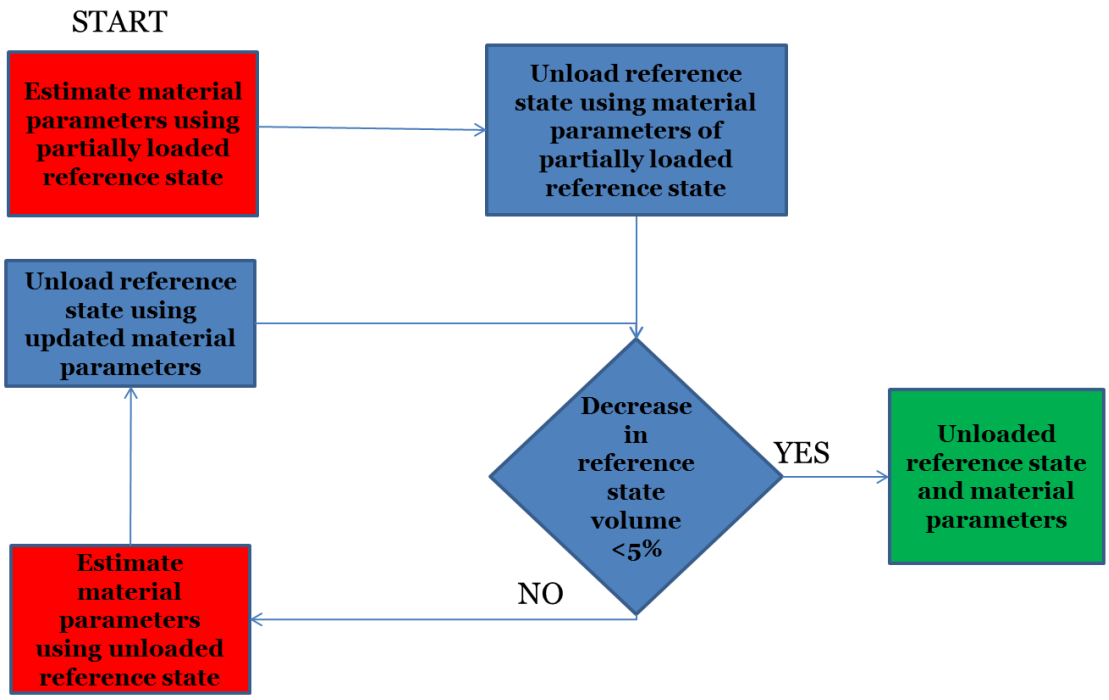

Figure 13: The flowchart of the unloading-parameter estimation scheme

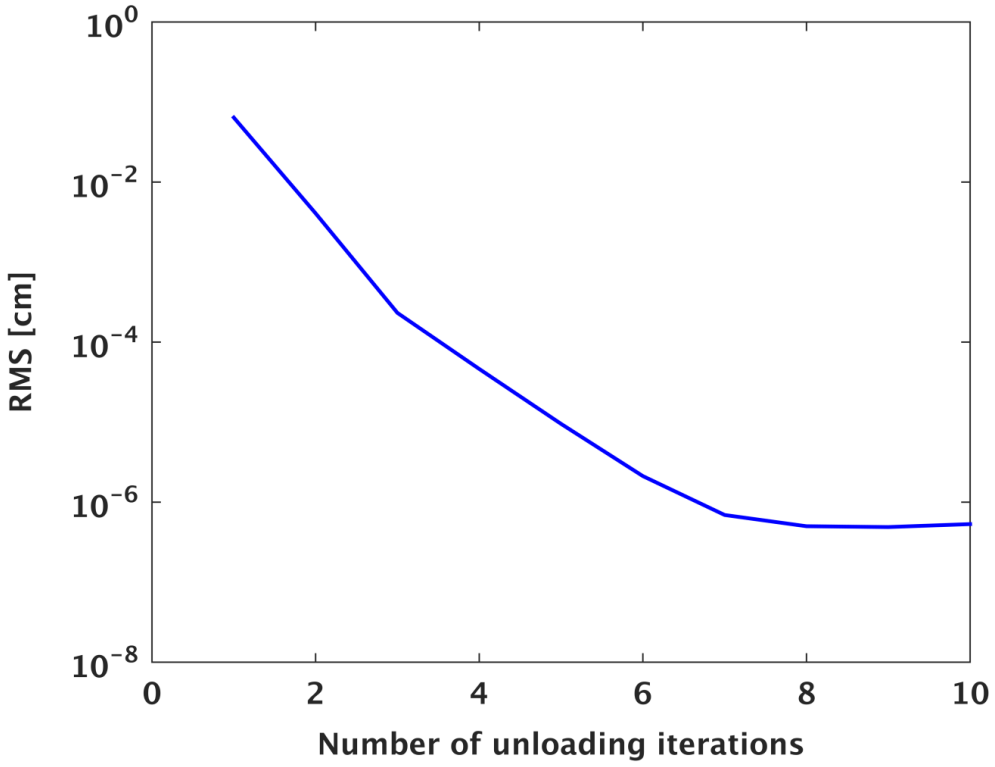

Figure 14: Root Mean Square (RMS) of distance between nodal points on epicardium and endocardium of inflated and target geometries (total of 1064 points)

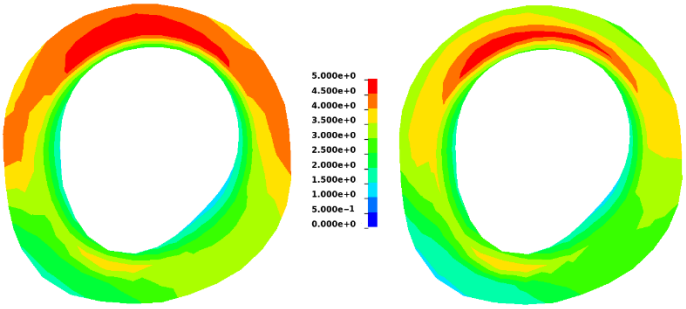

Figure 15: Contours of first principle stress (kPa) in a mid-ventricle slice at end-diastole before (left) and after (right) unloading

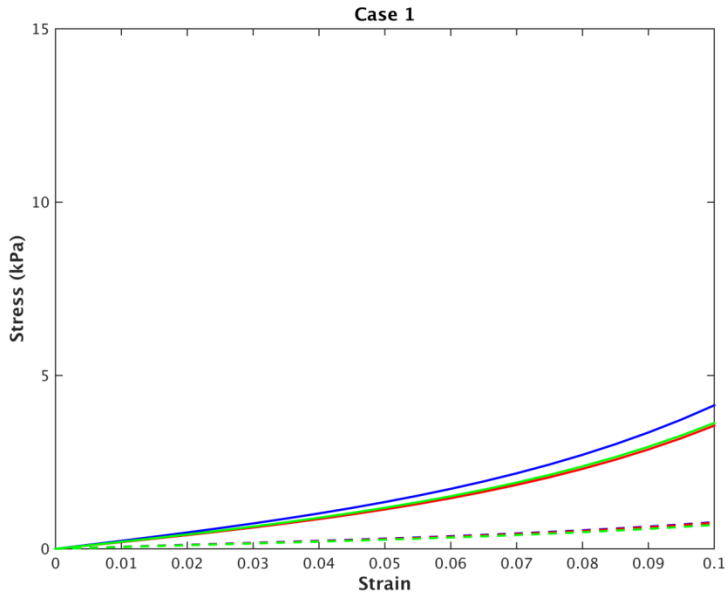

Figure 16: Biaxial stress vs. strain in fiber (solid lines) and transverse sheet (dashed lines) before unloading (blue) after first unloading (in red), after second unloading (in green) and after third unloading (in cyan, only for case 2 and 4)

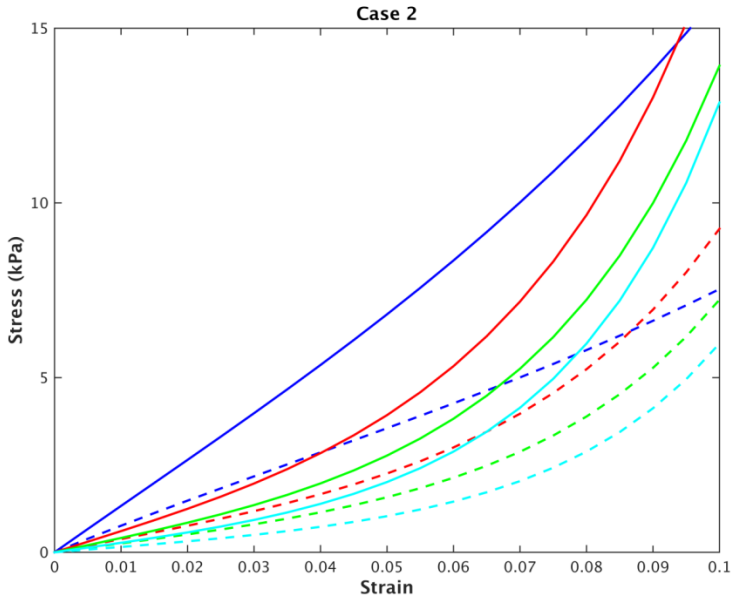

Figure 17: Biaxial stress vs. strain in fiber (solid lines) and transverse sheet (dashed lines) before unloading (blue) after first unloading (in red), after second unloading (in green) and after third unloading (in cyan, only for case 2 and 4)

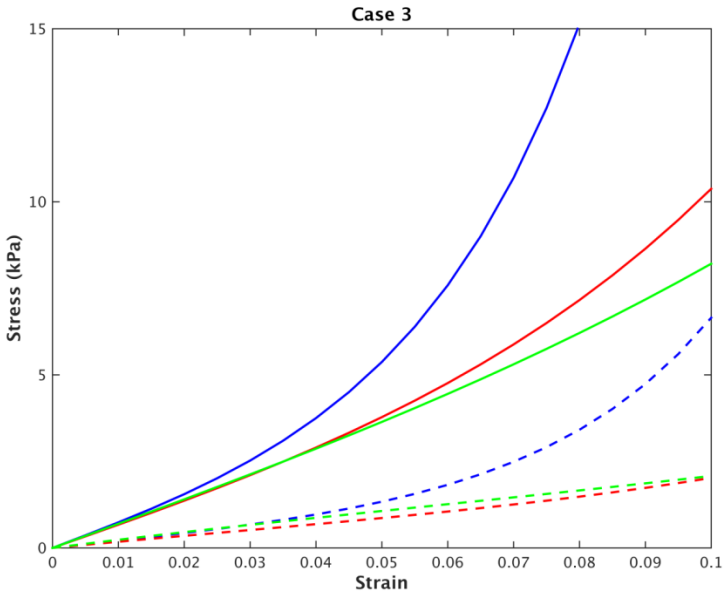

Figure 18: Biaxial stress vs. strain in fiber (solid lines) and transverse sheet (dashed lines) before unloading (blue) after first unloading (in red), after second unloading (in green) and after third unloading (in cyan, only for case 2 and 4)

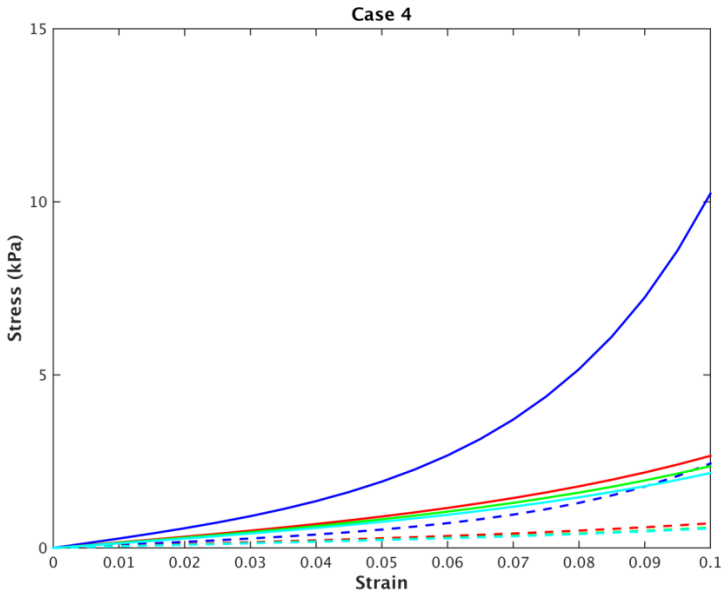

Figure 19: Biaxial stress vs. strain in fiber (solid lines) and transverse sheet (dashed lines) before unloading (blue) after first unloading (in red), after second unloading (in green) and after third unloading (in cyan, only for case 2 and 4)

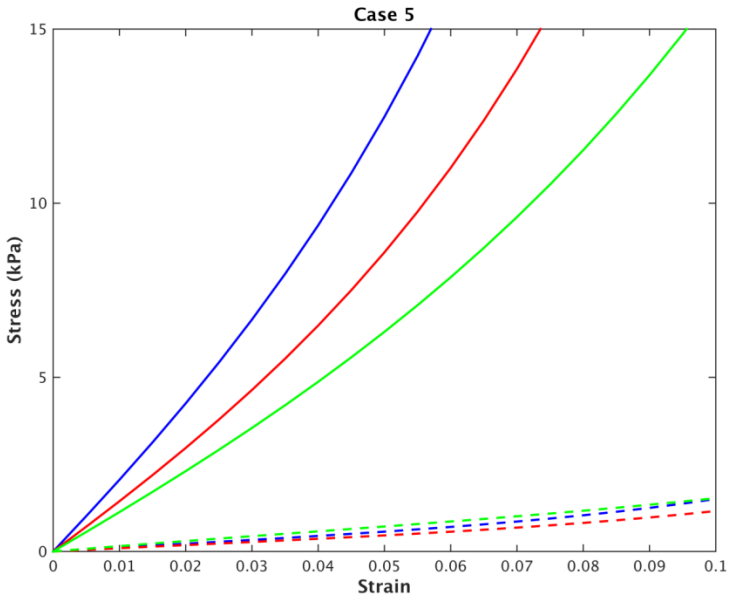

Figure 20: Biaxial stress vs. strain in fiber (solid lines) and transverse sheet (dashed lines) before unloading (blue) after first unloading (in red), after second unloading (in green) and after third unloading (in cyan, only for case 2 and 4)

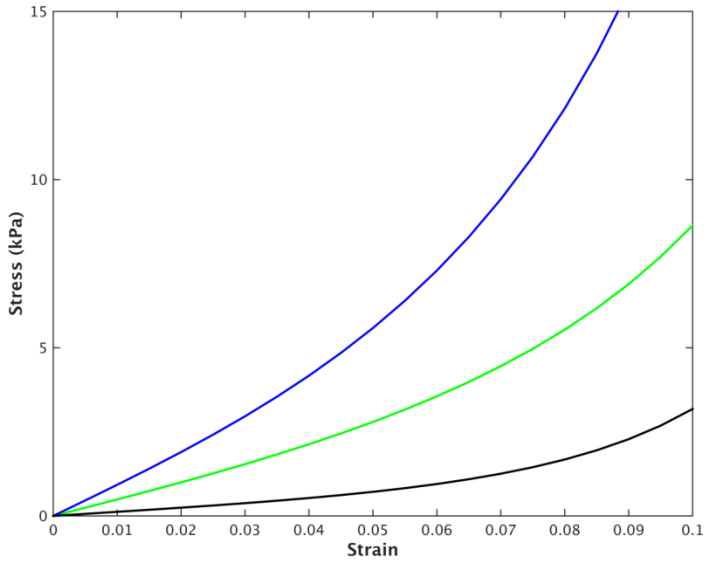

Figure 21: Average of five cases' myofiber stress vs. strain in a biaxial test, before unloading (in blue), after unloading (in green) and results of reference [47] (average of four cases)

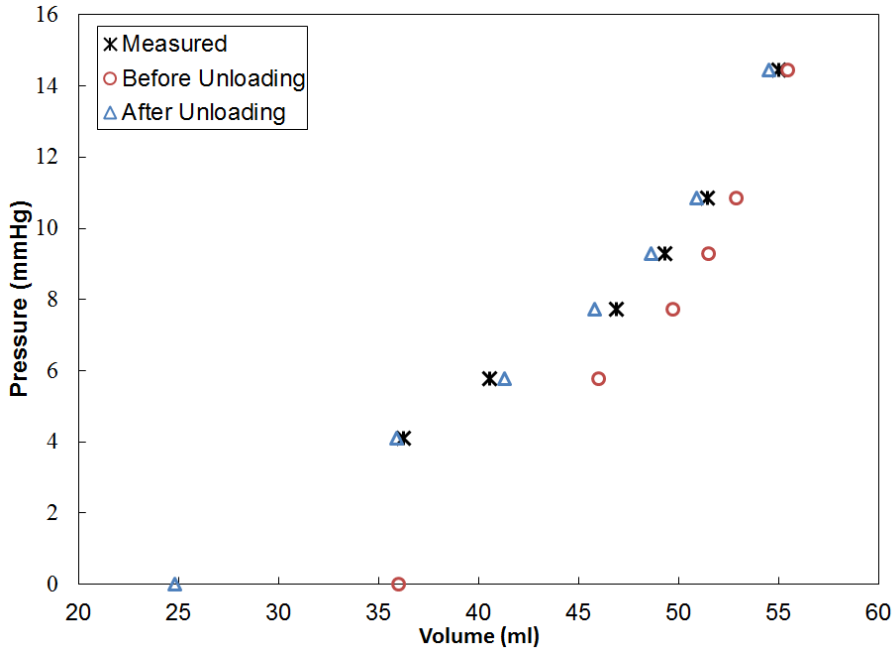

Figure 22: Comparison of experimentally measured LV pressure versus volume during diastole (case 4) to the values predicted by the models before and after unloading. Using the numerically unloaded reference state more precisely described the diastolic PV relationship.

Chapter Four: Myofiber Architecture Sensitivity Analysis

The goal of this study was to investigate the sensitivity of computational models of the heart to their incorporated myofiber architecture during diastole. This architecture plays a critical role in the mechanical and electrical function of the heart and changes after myocardial tissue remodeling, which is associated with some of the most common heart diseases. In the current study, a left ventricular finite element (FE) model of the porcine heart was created using magnetic resonance images (MRI), which represents the in-vivo geometry. Various myofiber architectures were assigned to the FE mesh, in the form of fiber and sheet angles. A structural based material law was used to model the behavior of passive myocardium and its parameters were estimated using measured in-vivo strains and cavity volume from MRI. The final results showed noticeable sensitivity of the stress distribution to both the fiber and sheet angle distributions. This implies that a structural based material law that take into account the effect of both fiber and sheet angle distributions should be used. The results also show that even though the simulation results improve by using available data from histological studies of myocardial structure, the need for individualized myofiber architecture data is crucial.

The myocardium of the left ventricle (LV) is predominantly composed of bundles of myofibers, which have s significant effect on both the mechanical and electrical function of the heart. The architecture of these myofibers has orientation angles that vary transmurally, which enables the heart to eject blood in the most efficient manner as it deforms [17]. Some of the first quantitative measurements of myofiber orientations were collected from canine ventricles [13]. Subsequent investigations showed that myocardial microstructure is composed of discrete layers, which run transmurally across the ventricular wall and are referred to as sheets [14, 15]. LeGrice et al. provided a more detailed and systematic account of the architecture of these sheets [16]. Finite element (FE) models of the heart incorporate constitutive laws that simulate the anisotropic and

nonlinear behavior of the myocardium, which rely on a description of myofiber architecture (i.e., the distribution of fiber and sheet orientation angles) [17].

A common approach to incorporate anisotropy of myocardium in FE models of the heart is to assume a uniform distribution of fiber and sheet angles based on the information obtained from histological studies [51, 52]. In order to create more realistic FE models of the heart, it is crucial to investigate the sensitivity of these models to myofiber architecture. Previously, Wang et al. [29] studied the sensitivity of a human LV model to changes in myofiber architecture. The FE model incorporated a structural based material law [17], which employed a set of material parameters that were taken from simple shear tests on specimens of excised pig heart previously reported by Dokos et al. [24]. The results of that study imply that the transmural distribution of myofiber stress and strain are highly sensitive to fiber angles distribution but insensitive to sheet angles. However, those results were taken from a single longitudinal region. In the current work, a comprehensive animal specific model is constructed to conduct a similar sensitivity study. Here the same constitutive law used in [29] was used to model healthy LV myocardium of a porcine heart in diastole. In order to use realistic animal specific material parameters in the constitutive model, in-vivo strains were measured from magnetic resonance imaging (MRI) and used for parameter estimation of the material law. A FE model was created from the in-vivo images of the LV and was assigned different combinations of fiber and sheet angles. Parameter estimation was performed by minimizing the difference between MRI measured and FE predicted strains and cavity volumes. Both were assess at the same end-diastolic pressure, which was measured via catheterization.

It should be noted that the same experimental MRI and pressure data, along with the modeling and optimization techniques, that were used in the previous two chapters were also employed in this study. Previously, Lee et al. [35] measured myofiber orientation angles in five in vitro porcine hearts and reported the transmural change of average myofiber angle with respect to the circumferential direction from -40° (at epicardium) to 80° (at endocardium). Myocyte sheet angles following the study of LeGrice et al. [16] on canine hearts varied from -45o (at epicardium) to +45o

(at endocardium) with respect to radial direction. In the current study, a custom MATLAB code was used to assign a linear distribution of myofiber and myocyte sheet orientation angles to each hexahedral element. It has been shown that a linear distribution of myofiber angles across the myocardium provides a relatively close match to DTMRI data [52]. In order to investigate the sensitivity of left ventricular response to changes of myofiber architecture, we assumed seven different transmural distributions of myofiber and sheet angles. Each set of angles was assigned to an identical FE model of a porcine LV (Table 8).

Parameters of the material law were estimated for each one of the FE models using the procedure described in Chapter 2 (total of 7 parameter estimation problems). The final MSE values are listed in Table 8. Upon inspection of the MSE values obtained from the structural based material law, it is clear that the MSE values vary when identical FE models with different myofiber architecture were used during the parameter estimation. The best fit was obtained when a distribution of -45° to 90° for the myofiber angle and a distribution of -45° to $+45^{\circ}$ for the sheet angle were used. Considering the variability between animals used in different studies, this result is consistent with the results of previous histological studies [16, 35]. In order to study the sensitivity of the stress distribution to myofiber architecture, the estimated parameters of the material law were used in FE models which were loaded to the same end-diastolic pressure. Figures 24-26 show the results of these FE simulations in the form of the circumferential distribution of myofiber stress at three regions of the LV model, i.e., near the base, mid-ventricle and apex. The stresses in these figures are the average of the three neighboring transmural elements (transmural average).

Based on the results of the current study (Figs. 24-26), the myofiber stress distribution is sensitive to both fiber and sheet angle distributions in several regions of the FE model of the in-vivo LV. Although the stresses are affected more by fiber angles compared to sheet angles, their dependence to sheet angles is not negligible. Notably, Wang et al. did not observe sensitivity of stresses to sheet angles in their study with FE models of a human LV [29]. This could be due to the fact that in that study, stress was only assessed at one longitudinal section of the LV model, i.e., the circumferential

stress distribution was not assessed. In the current study it can be seen that at multiple circumferential locations the fiber stress varies when the sheet angle distribution changes (where dashed lines in Figs. 24-26 deviate). The contribution of sheet angles on the myofiber stress distribution is due to terms in Eq. (11) that contain $\bar{I}_{4s}$ and $\bar{I}_{8fs}$(sheet and fiber-sheet coupling invariants). In contrast, constitutive laws that treat the myocardium as transversely isotropic relative to the local myofiber direction (for example see [21]) cannot capture the effect of variations of local myocyte sheet directions.

The results of this study show that the in-vivo stress distributions of the LV during diastole are sensitive to both fiber and sheet angle distributions. Therefore, precise patient-specific descriptions of myofiber architecture should be an essential part of a realistic computational model of the heart. The results of this study also imply that in order to have a more realistic computational simulation of myocardial mechanics, structural based material laws that take into account the effect of both myofiber and sheet angle distributions should be used.

Table 8: Seven variations of myofiber orientation and myocyte sheet angles assigned to the FE model (angles in degrees). Shaded cells represent average measured values from references [35] and [16].

Fiber angle at epicardium	Fiber angle at endocardium	Sheet angle at epicardium	Sheet angle at endocardium	MSE values
-20	40	-45	45	7.283
-30	60	-45	45	7.166
-40	80	-45	45	7.033
-45	90	-45	45	6.984
-70	90	-45	45	7.017
-40	80	-30	30	7.242
-40	80	-60	-60	6.999

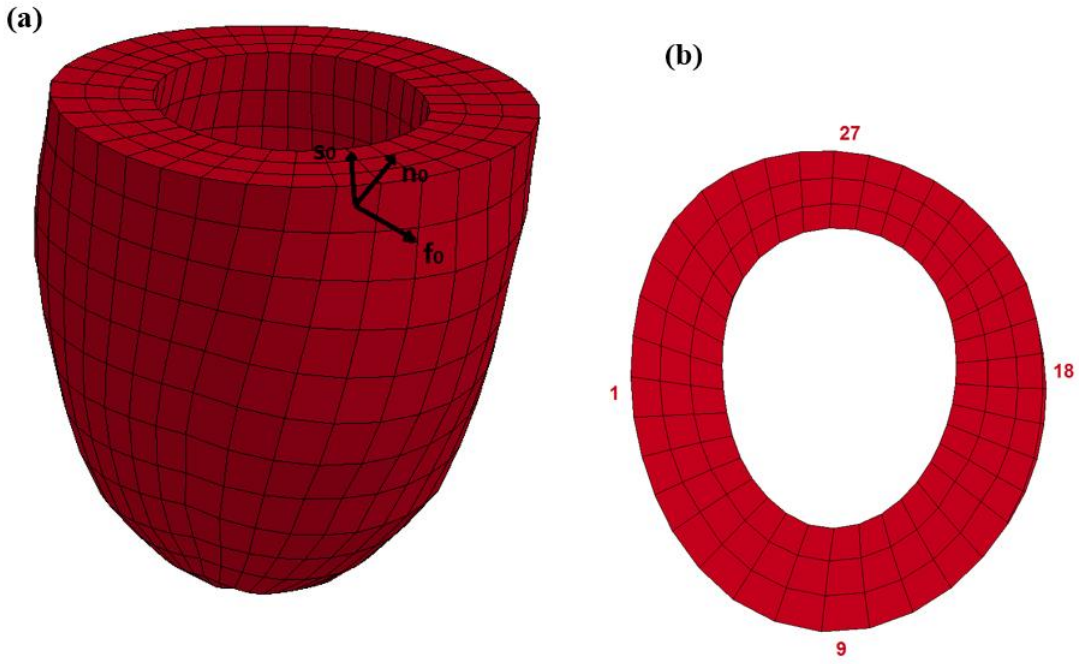

Figure 23: (a) The FE model of the LV used in this study. The local myofiber, sheet and normal angles incorporated in the structure based material law are shown in a representative element. (b) Short axis view of the FE model. Numbers indicate the circumferential location around the LV.

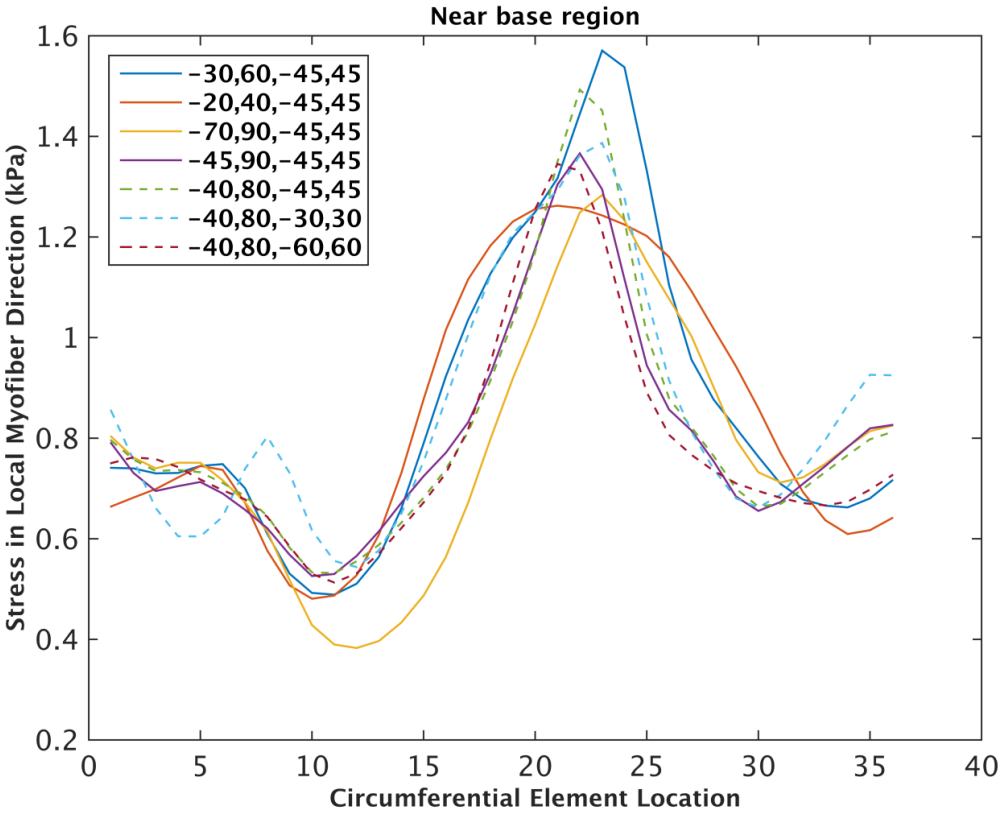

Figure 24: Circumferential distribution of fiber stress near base region. Stress was calculated as the average of three elements in the same circumferential location. Solid lines represent results of FE models in which only fiber angle distributions were deviated from measured experimental values and dashed lines represent results of FE models in which only sheet angle distributions were deviated from measured experimental values.

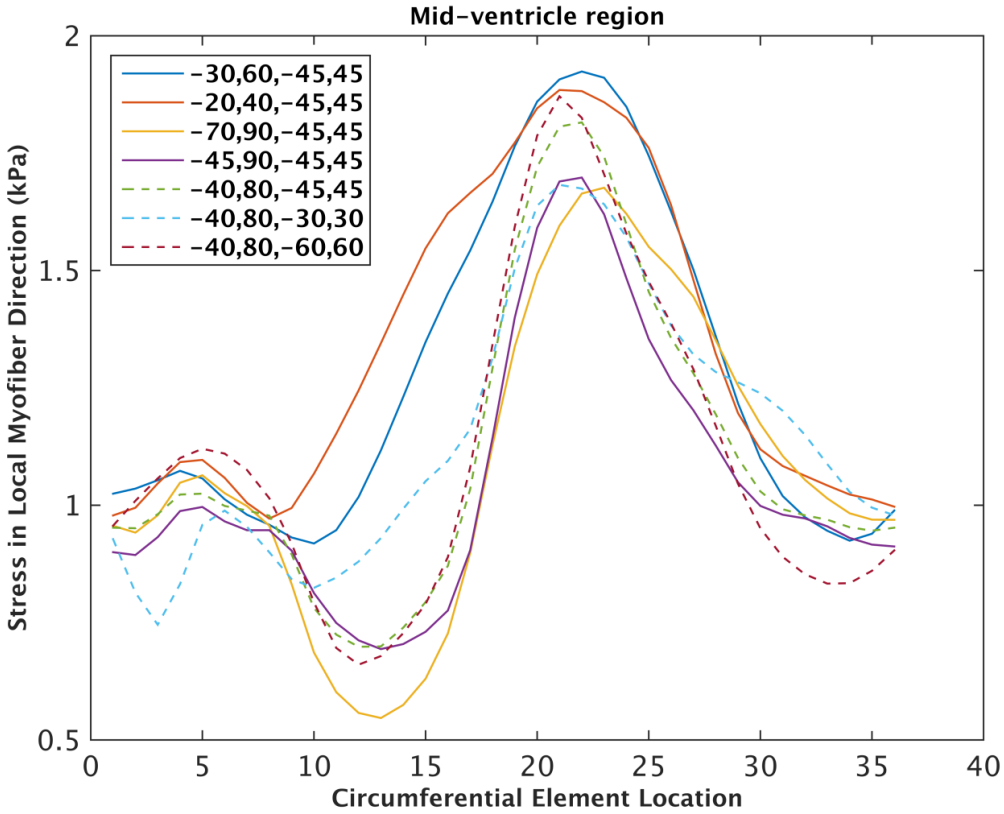

Figure 25: Circumferential distribution of fiber stress near mid-ventricle region. Stress was calculated as the average of three elements in the same circumferential location. Solid lines represent results of FE models in which only fiber angle distributions were deviated from measured experimental values and dashed lines represent results of FE models in which only sheet angle distributions were deviated from measured experimental values.

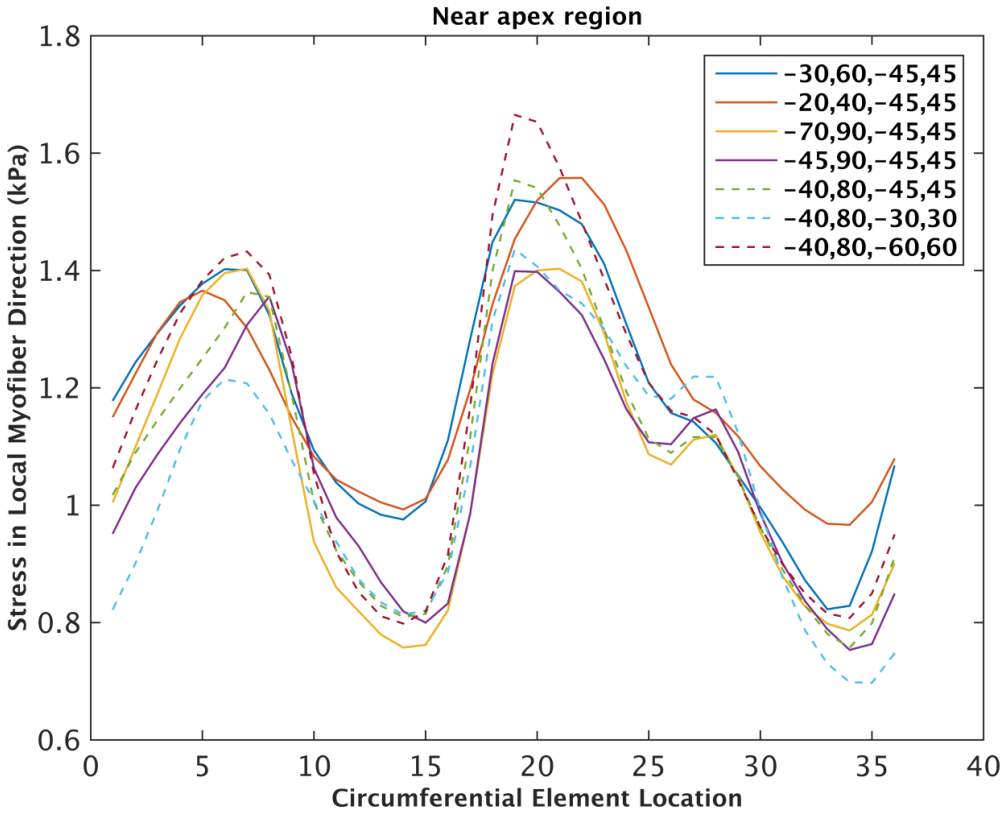

Figure 26: Circumferential distribution of fiber stress near apex region. Stress was calculated as the average of three elements in the same circumferential location. Solid lines represent results of FE models in which only fiber angle distributions were deviated from measured experimental values and dashed lines represent results of FE models in which only sheet angle distributions were deviated from measured experimental values.

Chapter Five: Modeling Heart Growth

Medical professionals usually classify heart failure into diastolic and systolic heart failure [53]. In diastolic heart failure, "ventricular chamber is unable to accept an adequate volume of blood during diastole at normal diastolic pressures and at volumes sufficient to maintain an appropriate stroke volume" [54]. Diastolic heart failure is followed by the thickening of the ventricular wall or concentric hypertrophy [55]. Systolic heart failure is "a condition in which the heart fails to discharge its contents adequately" [56]. Systolic heart failure is followed by the dilation of the ventricles or eccentric hypertrophy. Both conditions will seriously endanger the overall health and can be fatal. Heart failure is very sensitive to cardiac microstructure, geometry and loading, therefore predicting the timeline of heart failure for a specific patient is almost unattainable. Computational modeling of heart growth and remodeling is a powerful tool to predict the geometric changes during heart failure [57]. There are multiple growth models proposed by various research groups [57-60]. In the current study we used a recently developed growth model by Genet et al. [57] and adapted it with our finite element model of the left ventricle discussed in previous chapters.

In order to model growth, the deformation gradient tensor $\boldsymbol{F}$ was multiplicatively decomposed into an elastic part $\boldsymbol{F}^e$ and a growth part $\boldsymbol{F}^g$:

$$\boldsymbol{F} = \boldsymbol{F}^e \cdot \boldsymbol{F}^g \tag{32}$$

The growth model is conceptually modular and can easily be combined with various myocardial constitutive models. For convenience , we incorporated the constitutive model of Guccione et al. [21] in our growth model. In this manner, the elastic tensor $\boldsymbol{F}^e$ is equivalent to the regular elastic deformation gradient tensor $\boldsymbol{F}$ used to calculate stresses (see chapter 2). The total second Piola-Kirchhoff stress is calculated using chain rule as follows [57]:

$$\boldsymbol{S} = \frac{\partial \psi}{\partial \boldsymbol{E}} = \frac{\partial \psi}{\partial \boldsymbol{E}^e} : \frac{\partial \boldsymbol{E}^e}{\partial \boldsymbol{E}} = (\boldsymbol{F}^g)^{-1} \cdot \boldsymbol{S}^e \cdot (\boldsymbol{F}^g)^{-T} \tag{33}$$

Where $\boldsymbol{S}^e$ is the elastic second Piola-Kirchhoff stress obtained from Eq. (14), and ψ and $\boldsymbol{E}$ are the strain energy per unit volume of the reference configuration and Green-Lagrange strain respectively. We need to have $\boldsymbol{F}^g$ before we can calculate the Cauchy stress using Eq. (34):

$$\boldsymbol{\sigma} = \frac{1}{J} \boldsymbol{F} \cdot \boldsymbol{S} \cdot \boldsymbol{F}^T \tag{34}$$

In order to quantify transverse growth of the myocardium, a scalar valued growth multiplier $v^{\perp}$ is introduced to model parallel deposition of sarcomeres on the molecular level. The transverse growth tensor is defined as [57]:

$$\boldsymbol{F}^g = v^{\perp} \boldsymbol{I} + [1 - v^{\perp}] \boldsymbol{f}_0 \otimes \boldsymbol{f}_0 \tag{35}$$

Where $\boldsymbol{f}_0$ is the local myofiber direction in the reference configuration.

To quantify longitudinal growth of the myocardium another growth multiplier $v^{\parallel}$ is introduced to model serial decomposition of sarcomeres. The longitudinal growth tensor is defined as [57]:

$$\boldsymbol{F}^g = \boldsymbol{I} + [v^{\parallel} - 1] \boldsymbol{f}_0 \otimes \boldsymbol{f}_0 \tag{36}$$

It should be noted that $v^{\perp}, v^{\parallel} \geq 1$ and only growth multipliers greater than unity will result in growth, otherwise the growth tensor is equal to identity tensor. For simplicity, stretch driven kinetics are assumed for both growth mechanisms (transverse and longitudinal growth) [57]:

$$\dot{v} = \frac{1}{\tau} \langle \lambda - \lambda^{crit} \rangle \tag{37}$$

Where the terms in the Macaulay brackets are the current fiber stretch (stretch in the current configuration), $\lambda = [\boldsymbol{f}_0 . \boldsymbol{F}^t . \boldsymbol{F} . \boldsymbol{f}_0]^{1/2}$ and physiological stretch limit (λ^{crit}). We calculate λ^{crit} as

a regionally varying stretch under physiological conditions. The parameter τ is a scaling parameter in time which governs the growth rate (the smaller the value of τ the faster the growth rate and vice versa). The true value of this parameter is different for different animals and should be calibrated for a specific animal being studied.

The growth model was incorporated as a user defined material subroutine in the finite element solver LS-DYNA (Livermore Software Technology Corporation, Livermore, CA). In each time step, the ordinary differential equation in Eq. (37) is solved to obtain an update of the growth multiplier for each element. To solve this equation, a finite difference approximation of the first order time derivative is used as $\dot{v} = [v - v_n]/\Delta t$ where v_n denotes the growth multiplier of the previous time step and $\Delta t = t - t_n$ is the current time increment. Consequently, the growth multiplier of the current time step is explicitly updated using Eq. (34):

$$v = v_n + \langle \lambda - \lambda^{crit} \rangle \frac{\Delta t}{\tau} \tag{38}$$

The critical stretches (λ^{crit}) were calculated after applying the physiological end-diastolic pressure on a left ventricular model of a healthy porcine heart (baseline model). Then the regionally varying values of critical stretch λ^{crit} were saved in the FE input deck (one stretch value for each element). These stretches are invoked in each call of the user defined material subroutine to calculate the growth multiplier. It should be noted that if during the finite element solution, the current stretch value of an element doesn't exceed the critical stretch value the growth multiplier for that element will not change. The flowchart of user defined material subroutine for modeling growth is shown in Figure 27. In order to trigger growth, we applied an end-diastolic pressure overload on the finite element model. We applied a pressure load two times the physiological end-diastolic pressure and kept the pressure load constant to allow for growth evolution and finally unload the model to zero pressure (Fig. 28).

The time step in Eq. (38) was taken identical to the finite element solver time step. The value of scaling parameter τ is not reported for pig heart in literature; therefor we tried various values to reach a rough approximation. Using very small values of τ, the finite element model will grow unrealistically fast; on the other hand, using very large values of τ the resulting growth will not be visible. Following the calculation of the growth multiplier, the growth tensor $\boldsymbol{F}^g$ is constructed using either Eq. (37) or Eq. (38) depending on which growth model is chosen in the input deck (a flag was defined in the user defined material subroutine to choose between transverse and longitudinal growth models in the finite element input deck). Subsequently, the elastic tensor $\boldsymbol{F}^e$ is calculated using Eq. (32):

$$\boldsymbol{F}^e = \boldsymbol{F} \cdot \boldsymbol{F}^{g\,-1} \tag{35}$$

It should be noted that only $\boldsymbol{F}$ is the gradient of a continuous mapping and two other tensors (the elastic tensor $\boldsymbol{F}^e$ and the growth tensor $\boldsymbol{F}^g$) generally cannot be derived as gradient from a vector field. Additionally, only elastic deformation generates stress, therefor the strain energy function is a function of elastic deformation only [57]. In the next step the elastic tensor $\boldsymbol{F}^e$ is fed into the hyper-elastic constitutive model to update the stress. The resulting stresses are used to calculate new deformations. Fig. 30-31 show some qualitative results of a single finite element solution in which the growth module was triggered due to pressure overload.

The simulation presented in this chapter was a rudimentary growth model and in order to get reliable results that predict real growth in animal heart it needs further refinement. For example, the ordinary differential equation (Eq. (37)) which represents the kinetics of the growth should be replaced with a more elaborate equation that caps the maximum growth [58], involves reverse growth [60] or is stress dependent (for stress-driven growth modeling) [61]. Additionally, in our

simulation the value of parameter τ was based on some computational experiments that resulted in a qualitative representation of growth. To develop an animal specific growth model, the value of this parameter should be estimated for that animal. These details will be the subject of future investigations in our lab.

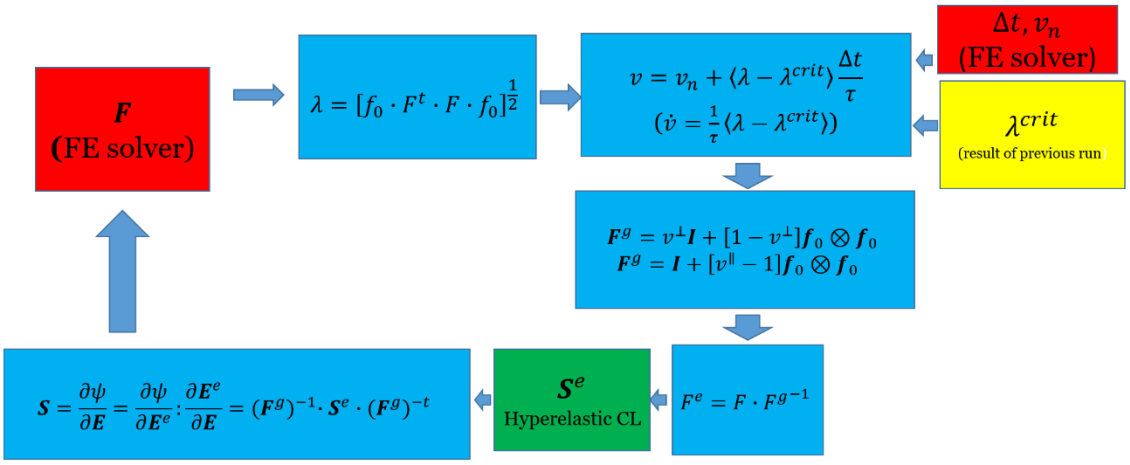

Figure 27: The flowchart of user defined material subroutine for modeling growth

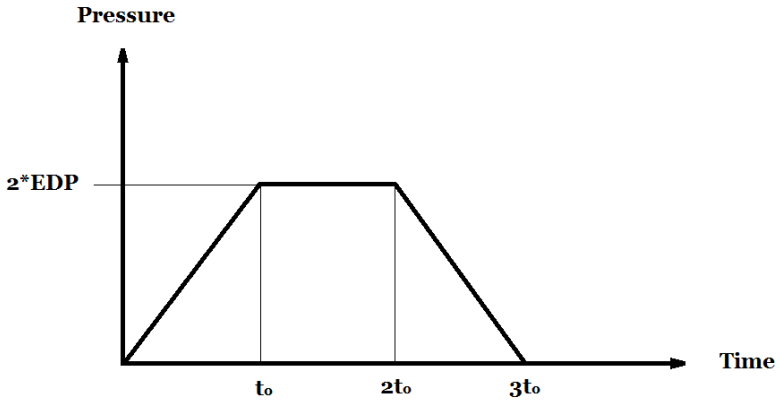

Figure 28: The ventricle is loaded to a pressure two times the physiological end-diastolic pressure, then allowed to grow for a duration and then unloaded

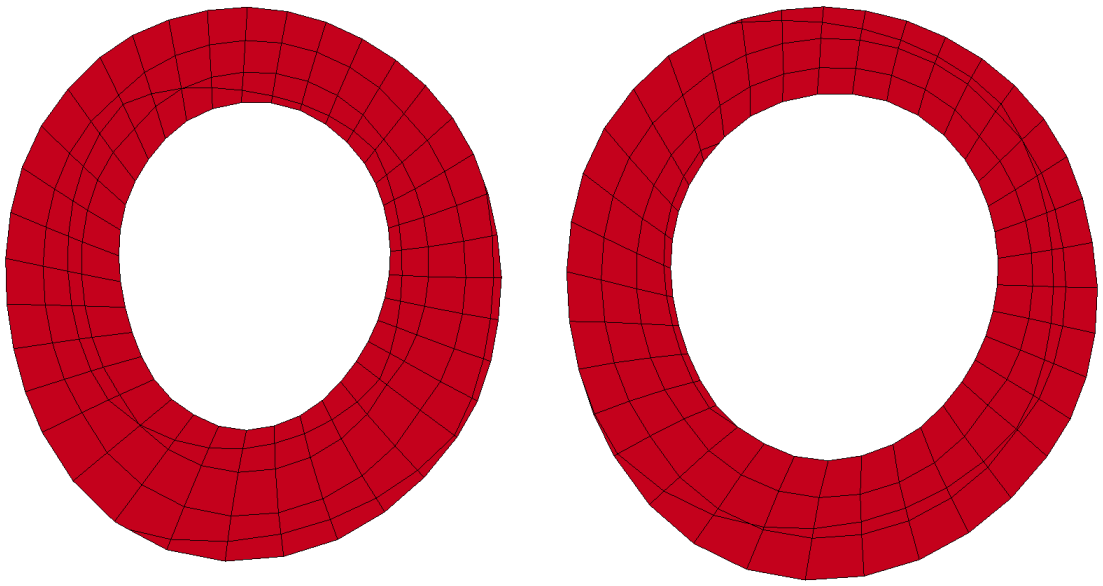

Figure 29: Short axis view of a mid-slice of the finite element model before (left) and after growth (right), myocardial wall thickness decreased because the longitudinal growth tensor was used (Eq. (36))

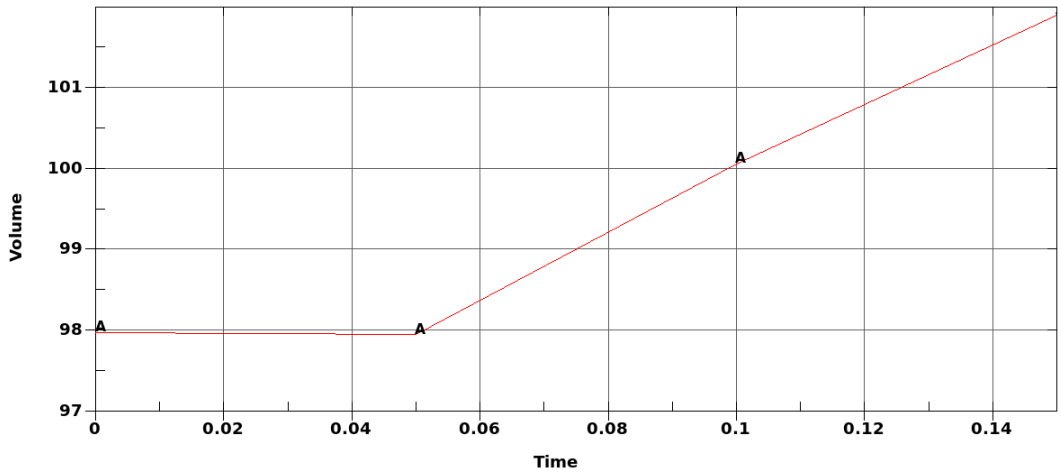

Figure 30: Total elements' volume versus time; growth triggers at t=0.05

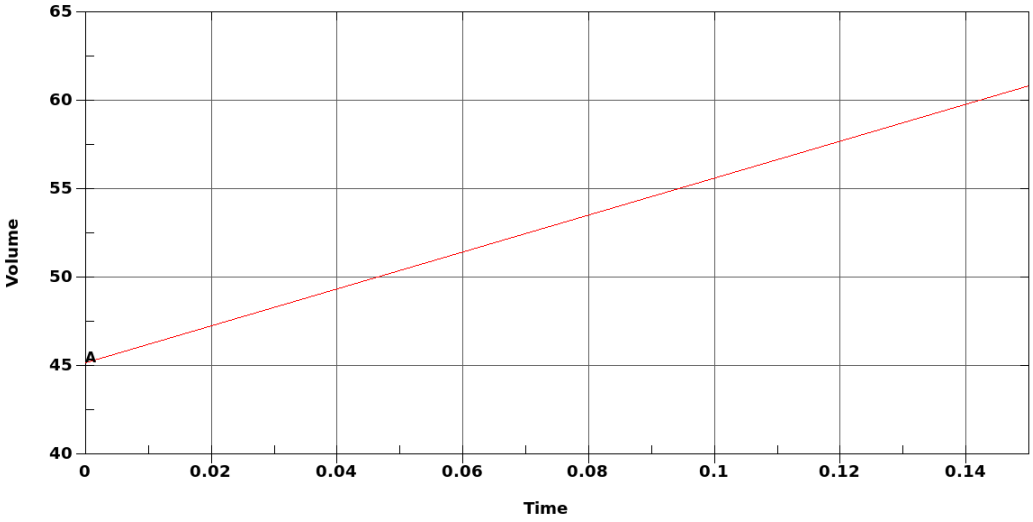

Figure 31: Cavity volume versus time

Chapter Six: Conclusion

In chapter two, a newly developed structural constitutive model was incorporated in the finite element solver as a user defined material subroutine. Using four MRI data sets, we showed that using this constitutive model would approximate the physiological behavior of the heart more accurately during simulation. In chapter three, we implemented a previously reported numerical technique to unload the geometry of the heart from its partially loaded geometry obtained from imaging of the beating heart. We showed that when these unloaded geometries were used as the reference state of the finite element simulations, the resulting estimated material parameters would be more accurate. In chapter 4, we used computational model developed in chapters 2 and 3 to study the sensitivity of the computational model to myofiber structure. Finally in chapter 5, a stretch driven continuum growth model was incorporated in the finite element solver which was one of the first steps of growth modeling in our lab and needs further refinement and development.

In future investigations the computational model we presented here will be further refined and developed toward a patient specific computational model that could be used in clinical settings. For example, currently the material parameters estimation is based on using specialized MRI techniques that a human patient would not usually experience in clinic. Pressure catheterization is also not a regular clinical practice for measuring heart pressure. Additionally, in order to have a comprehensive and realistic computer model of the heart, the left ventricular models should be extended to biventricular and ultimately whole heart models that contain all four chambers of the heart and its valves. Obviously, these goals cannot be achieved in a single dissertation but will create fascinating research opportunities for the new graduate students and research fellows in our lab.

References

1. LeGrice, I., P. Hunter, and B. Smaill, *Laminar structure of the heart: a mathematical model.* American Journal of Physiology-Heart and Circulatory Physiology, 1997. **272**(5): p. H2466-H2476.
2. Wenk, J.F., et al., *A method for automatically optimizing medical devices for treating heart failure: designing polymeric injection patterns.* J Biomech Eng, 2009. **131**(12): p. 121011.
3. Wenk, J.F., et al., *First finite element model of the left ventricle with mitral valve: insights into ischemic mitral regurgitation.* Ann Thorac Surg, 2010. **89**(5): p. 1546-53.
4. Sun, K., et al., *Dor procedure for dyskinetic anteroapical myocardial infarction fails to improve contractility in the border zone.* The Journal of thoracic and cardiovascular surgery, 2010. **140**(1): p. 233-239. e4.
5. Wenk, J.F., P. Papadopoulos, and T.I. Zohdi, *Numerical modeling of stress in stenotic arteries with microcalcifications: a micromechanical approximation.* Journal of biomechanical engineering, 2010. **132**(9): p. 091011.
6. Wenk, J.F., et al., *A novel method for quantifying the in-vivo mechanical effect of material injected into a myocardial infarction.* Ann Thorac Surg, 2011. **92**(3): p. 935-41.
7. Wenk, J.F., et al., *Regional left ventricular myocardial contractility and stress in a finite element model of posterobasal myocardial infarction.* Journal of biomechanical engineering, 2011. **133**(4): p. 044501.
8. Klepach, D., et al., *Growth and remodeling of the left ventricle: A case study of myocardial infarction and surgical ventricular restoration.* Mechanics research communications, 2012. **42**: p. 134-141.
9. Wriggers, P., *Nonlinear finite element methods*. 2008: Springer Science & Business Media.
10. Young, A., et al., *Extended confocal microscopy of myocardial laminae and collagen network.* Journal of Microscopy, 1998. **192**(2): p. 139-150.
11. Sands, G.B., et al., *Automated imaging of extended tissue volumes using confocal microscopy.* Microscopy research and technique, 2005. **67**(5): p. 227-239.
12. Gilbert, S.H., et al., *Regional localisation of left ventricular sheet structure: integration with current models of cardiac fibre, sheet and band structure.* European journal of cardio-thoracic surgery, 2007. **32**(2): p. 231-249.
13. Streeter, D.D., et al., *Fiber orientation in the canine left ventricle during diastole and systole.* Circulation research, 1969. **24**(3): p. 339-347.
14. Spotnitz, H.M., et al., *Cellular basis for volume related wall thickness changes in the rat left ventricle.* Journal of molecular and cellular cardiology, 1974. **6**(4): p. 317-331.
15. Grimm, A., et al., *Fiber bundle direction in the mammalian heart.* Basic research in cardiology, 1976. **71**(4): p. 381-388.
16. LeGrice, I.J., et al., *Laminar structure of the heart: ventricular myocyte arrangement and connective tissue architecture in the dog.* American Journal of Physiology-Heart and Circulatory Physiology, 1995. **38**(2): p. H571.
17. Holzapfel, G.A. and R.W. Ogden, *Constitutive modelling of passive myocardium: a structurally based framework for material characterization.* Philos Trans A Math Phys Eng Sci, 2009. **367**(1902): p. 3445-75.
18. Hunter, P.J. and B.H. Smaill, *The analysis of cardiac function: a continuum approach.* Progress in biophysics and molecular biology, 1988. **52**(2): p. 101-164.

19. Humphrey, J. and F. Yin, *On constitutive relations and finite deformations of passive cardiac tissue: I. A pseudostrain-energy function.* Journal of biomechanical engineering, 1987. **109**(4): p. 298-304.
20. Humphrey, J., R. Strumpf, and F. Yin, *Determination of a constitutive relation for passive myocardium: I. A new functional form.* Journal of biomechanical engineering, 1990. **112**(3): p. 333-339.
21. Guccione, J., A. McCulloch, and L. Waldman, *Passive material properties of intact ventricular myocardium determined from a cylindrical model.* Journal of biomechanical engineering, 1991. **113**(1): p. 42-55.
22. COSTA, K., et al., *A three-dimensional finite element method for large elastic deformations of ventricular myocardium: II-prolate spheroidal coordinates.* Journal of biomechanical engineering, 1996. **118**(4): p. 464-472.
23. Kerckhoffs, R., et al., *Homogeneity of cardiac contraction despite physiological asynchrony of depolarization: a model study.* Annals of biomedical engineering, 2003. **31**(5): p. 536-547.
24. Dokos, S., et al., *Shear properties of passive ventricular myocardium.* American Journal of Physiology-Heart and Circulatory Physiology, 2002. **283**(6): p. H2650-H2659.
25. Hunter, P., M. Nash, and G. Sands, *Computational electromechanics of the heart.* Computational biology of the heart, 1997. **12**: p. 347-407.
26. Schmid, H., et al., *Myocardial material parameter estimation—a comparative study for simple shear.* Journal of biomechanical engineering, 2006. **128**(5): p. 742-750.
27. Holzapfel, G.A., *Nonlinear solid mechanics*. Vol. 24. 2000: Wiley Chichester.
28. Göktepe, S., et al., *Computational modeling of passive myocardium.* International Journal for Numerical Methods in Biomedical Engineering, 2011. **27**(1): p. 1-12.
29. Wang, H.M., et al., *Structure-based finite strain modelling of the human left ventricle in diastole.* Int j numer method biomed eng, 2013. **29**(1): p. 83-103.
30. Wang, H., et al., *A modified Holzapfel-Ogden law for a residually stressed finite strain model of the human left ventricle in diastole.* Biomechanics and modeling in mechanobiology, 2014. **13**(1): p. 99-113.
31. Baillargeon, B., et al., *The Living Heart Project: A robust and integrative simulator for human heart function.* European Journal of Mechanics - A/Solids, 2014. **48**(0): p. 38-47.
32. Krishnamurthy, A., et al., *Patient-specific models of cardiac biomechanics.* Journal of computational physics, 2013. **244**: p. 4-21.
33. Gao, H., et al., *Parameter Estimation of the Holzapfel-Ogden Law for Healthy Myocardium.* Journal of Engineering Mathematics, 2014.
34. Mojsejenko, D., et al., *Estimating passive mechanical properties in a myocardial infarction using MRI and finite element simulations.* Biomechanics and modeling in mechanobiology, 2014: p. 1-15.
35. Lee, W.-N., et al., *Mapping myocardial fiber orientation using echocardiography-based shear wave imaging.* Medical Imaging, IEEE Transactions on, 2012. **31**(3): p. 554-562.
36. Gasser, T.C., R.W. Ogden, and G.A. Holzapfel, *Hyperelastic modelling of arterial layers with distributed collagen fibre orientations.* J R Soc Interface, 2006. **3**(6): p. 15-35.
37. Sun, K., et al., *A computationally efficient formal optimization of regional myocardial contractility in a sheep with left ventricular aneurysm.* Journal of biomechanical engineering, 2009. **131**(11): p. 111001.
38. Nair, A.U., D.G. Taggart, and F.J. Vetter, *Optimizing cardiac material parameters with a genetic algorithm.* Journal of biomechanics, 2007. **40**(7): p. 1646-1650.
39. Klotz, S., et al., *Single-beat estimation of end-diastolic pressure-volume relationship: a novel method with potential for noninvasive application.* American Journal of Physiology-Heart and Circulatory Physiology, 2006. **291**(1): p. H403-H412.

40. Xi, J., et al., *The estimation of patient-specific cardiac diastolic functions from clinical measurements.* Medical image analysis, 2013. **17**(2): p. 133-146.
41. Wenk, J.F., et al., *First evidence of depressed contractility in the border zone of a human myocardial infarction.* The Annals of thoracic surgery, 2012. **93**(4): p. 1188-1193.
42. Sermesant, M. and R. Razavi, *Personalized computational models of the heart for cardiac resynchronization therapy*, in *Patient-specific modeling of the cardiovascular system*. 2010, Springer. p. 167-182.
43. Rajagopal, V., et al. *Finite element modelling of breast biomechanics: directly calculating the reference state*. in *Engineering in Medicine and Biology Society, 2006. EMBS'06. 28th Annual International Conference of the IEEE*. 2006. IEEE.
44. Alastrué, V., et al., *Numerical framework for patient-specific computational modelling of vascular tissue.* International Journal for Numerical Methods in Biomedical Engineering, 2010. **26**(1): p. 35-51.
45. Bols, J., et al., *A computational method to assess the in vivo stresses and unloaded configuration of patient-specific blood vessels.* Journal of Computational and Applied Mathematics, 2013. **246**: p. 10-17.
46. Xi, J., et al., *Myocardial transversely isotropic material parameter estimation from in-silico measurements based on a reduced-order unscented Kalman filter.* Journal of the mechanical behavior of biomedical materials, 2011. **4**(7): p. 1090-1102.
47. Augenstein, K.F., et al., *Estimation of cardiac hyperelastic material properties from MRI tissue tagging and diffusion tensor imaging*, in *Medical Image Computing and Computer-Assisted Intervention–MICCAI 2006*. 2006, Springer. p. 628-635.
48. Okamoto, R., et al., *Epicardial suction: a new approach to mechanical testing of the passive ventricular wall.* Journal of biomechanical engineering, 2000. **122**(5): p. 479-487.
49. Walker, J.C., et al., *MRI-based finite-element analysis of left ventricular aneurysm.* American Journal of Physiology-Heart and Circulatory Physiology, 2005. **289**(2): p. H692-H700.
50. Helm, P., et al., *Measuring and mapping cardiac fiber and laminar architecture using diffusion tensor MR imaging.* Annals of the New York Academy of Sciences, 2005. **1047**(1): p. 296-307.
51. Potse, M., et al., *A comparison of monodomain and bidomain reaction-diffusion models for action potential propagation in the human heart.* Biomedical Engineering, IEEE Transactions on, 2006. **53**(12): p. 2425-2435.
52. Bishop, M.J., et al., *Comparison of rule-based and DTMRI-derived fibre architecture in a whole rat ventricular computational model*, in *Functional Imaging and Modeling of the Heart*. 2009, Springer. p. 87-96.
53. Chatterjee, K. and B. Massie, *Systolic and diastolic heart failure: differences and similarities.* Journal of cardiac failure, 2007. **13**(7): p. 569-576.
54. Zile, M.R. and D.L. Brutsaert, *New concepts in diastolic dysfunction and diastolic heart failure: Part I Diagnosis, prognosis, and measurements of diastolic function.* Circulation, 2002. **105**(11): p. 1387-1393.
55. Grossman, W., D. Jones, and L. McLaurin, *Wall stress and patterns of hypertrophy in the human left ventricle.* Journal of Clinical Investigation, 1975. **56**(1): p. 56.
56. Research, U.C.H.D.o.C. and S.T. LEWIS, *Diseases of the Heart... By Sir Thomas Lewis*. 1937: Macmillan & Company.
57. Genet, M., et al., *Modeling Pathologies of Diastolic and Systolic Heart Failure.* Annals of biomedical engineering, 2015: p. 1-16.
58. Kerckhoffs, R.C., J.H. Omens, and A.D. McCulloch, *A single strain-based growth law predicts concentric and eccentric cardiac growth during pressure and volume overload.* Mechanics research communications, 2012. **42**: p. 40-50.

59. Göktepe, S., O.J. Abilez, and E. Kuhl, *A generic approach towards finite growth with examples of athlete's heart, cardiac dilation, and cardiac wall thickening.* Journal of the Mechanics and Physics of Solids, 2010. **58**(10): p. 1661-1680.
60. Lee, L., et al., *A computational model that predicts reverse growth in response to mechanical unloading.* Biomechanics and modeling in mechanobiology, 2015. **14**(2): p. 217-229.
61. Rodriguez, E.K., A. Hoger, and A.D. McCulloch, *Stress-dependent finite growth in soft elastic tissues.* Journal of biomechanics, 1994. **27**(4): p. 455-467.

Vita

Amir Nikou

Tehran Polytechnic, Tehran, Iran MS in Aerospace Engineering, 2012

Isfahan University of Technology, Isfahan, Iran BS in Mechanical Engineering, 2006

Publications:

1. Dorsey, S. M., McGarvey, J. R., Wang, H, **Nikou, A**., Arama, L, Koomalsingh, K. J., Kondo, N., Gorman, J. H., Pilla, J. J and Gorman, R. C., 2015, "MRI Evaluation of Injectable Hyaluronic Acid-Based Hydrogel Therapy to Limit Ventricular Remodeling after Myocardial Infarction", *Biomaterials*, 69, pp. 65-75.

2. **Nikou, A**., Dorsey, S. M., Gorman III, J. H., Burdick, J. A., Pilla, J. J., Gorman, R. C., & Wenk, J. F., 2015, "Computational Modeling of Healthy Myocardium in Diastole" *Annals of Biomedical Engineering*, DOI: 10.1007/s10439-015-1403-7 (in press).

3. McGarvey, J. R., Mojsejenko, D., Dorsey, S. M., **Nikou, A.**, Burdick, J. A., Gorman III, J. H., Jackson, B. M., Pilla, J. J., Gorman, R. C., & Wenk, J. F., 2015, "Temporal Changes in Infarct Material Properties: An In Vivo Assessment Using Magnetic Resonance Imaging and Finite Element Simulations", *Annals of Thoracic Surgery*, 100(2), pp. 582-589.